Journal of Statistical Physics, Vol. 64, Nos. 3/4, 1991

Spatiotemporal Analysis of Complex Signals: Theory and Applications

Nadine Aubry,[1] Régis Guyonnet,[2] and Ricardo Lima[2,3]

Received August 28, 1990; final January 7, 1991

We present a space-time description of regular and complex phenomena which consists of a decomposition of a spatiotemporal signal into orthogonal temporal modes that we call chronos and orthogonal spatial modes that we call topos. This permits the introduction of several characteristics of the signal, three characteristic energies and entropies (one temporal, one spatial, and one global), and a characteristic dimension. Although the technique is general, we concentrate on its applications to hydrodynamic problems, specifically the transition to turbulence. We consider two cases of application: a coupled map lattice as a dynamical system model for spatiotemporal complexity and the open flow instability on a rotating disk. In the latter, we show a direct relation between the global entropy and the different instabilities that the flow undergoes as Reynolds number increases.

KEY WORDS: Spatiotemporal complexity; spatiotemporal chaos; signal analysis; Liapunov exponents; coupled map lattices; turbulence; transition to turbulence.

INTRODUCTION

The recent application of dynamical systems and bifurcation theory to the field of hydrodynamics has provided a reasonable understanding of transition to turbulence in severely closed flow systems such as Taylor–Couette and Rayleigh–Bénard flows. In these systems, disorder occurs only temporally, since the spatial structure of the system is quasifrozen by the confined boundaries. In these cases, indeed, there seems to be a close

---

[1] Benjamin Levich Institute and Department of Mechanical Engineering, City College of the City University of New York, New York, New York 10031.

[2] Centre National de la Recherche Scientifique, Centre de Physique Théorique, Luminy, Case 907, 13288 Marseille, France. Laboratoire Propre CNRS.

[3] Institute for Scientific Interchange, 10133 Torino, Italy.

0022-4715/91/0800-0683$06.50/0

connection between low-dimensional dynamics and fluid behavior and yet some "theoretical" routes to chaos have been identified in well-controlled experiments. These routes are period doubling (of which some universal characteristics have been described by Feigenbaum(23)), quasiperiodicity (in which a T^k torus becomes unstable, as shown by Ruelle and Takens(60) and Newhouse *et al.*(53)), and intermittency, first described by Pomeau and Manneville.(54) For examples, the first route has been observed by Libchaber *et al.*(42) in 2D Bénard convection, the second one has been identified by Gollub and Swinney(28) in Taylor–Couette flow, and the third one has been found by Bergé *et al.*(10) in a convection experiment.

The situation, however, is not so clear as the degree of confinement decreases and spatial disorder develops rapidly. Then, a large number of time and space scales become dynamically involved (often intermittently), even close to transition. From the theoretical point of view, notice that this intermittent regime in low-dimensional dynamical systems is present even in the most chaotic situation (mixing), as, for instance, in certain billiards problems, where periods of regular motion (as the ball is close to the wall) alternate with periods of random motion.(13) In the transitional phase, a typical regime seems to be spatiotemporal intermittency (STI), a mixture of organized "laminar" regions and disorganized "turbulent" spots. As the system evolves away from the critical point, the "turbulent" islands seem to invade the full flow domain and become more and more frequent. Thus, disorder is both spatial and temporal in the transition process from laminar to turbulent flow in (relatively) spatially large domains, and the standard dynamical systems approach, which takes into account temporal dynamics only, becomes almost useless. Another approach is needed. A statistical mechanics description has been often proposed,(55) but the construction of such a theory for systems which present space-time complexity is still an open question.

A large number of theoretical models has been developed to understand one dimensional (1D) spatiotemporal intermittency in (spatially) extended systems. These include coupled map lattices(14,34) and 1D partial differential equations (essentially the Kuramoto–Sivashinsky equation and the Ginzburg–Landau equation). Quasi-1D experiments have been specifically designed to study Rayleigh–Bénard convection in 1D annular geometry(9,19) for comparison between models and experiments. Although both numerical and experimental data display STI, the comparison suffers from the lack of tools to study space-time complexity. For example, there is no spatiotemporal equivalent to a dimension or an entropy as defined in temporal chaos. Moreover, Fourier analysis is no longer of much use since a large number of modes appear at the instability threshold.

As is well known, spatiotemporal intermittency and disorder do not occur only in transition phenomena, but they are ubiquitously present in all fully developed turbulent flows. Here, STI manifests itself in terms of the so-called "coherent structures" (CS) and their "intermittent" dynamics which have been visualized for a large number of years. Although most theoretical models treat turbulence as a purely random process, the importance of organized patterns has been shown to be of primary importance in generation, transport, and maintenance of turbulence. They have also permitted a great advance in turbulence control.(43) Despite an enormous amount of research in this area,(1, 11, 16, 32, 33, 47, 58, 71) the shape of these patterns as well as their evolution in time are still not well understood. There is thus no formulation to include CS into theoretical and numerical models of fully developed turbulent flows. One of the first attempts is that of Aubry *et al.*(4) (see also Aubry and Sanghi(5)), who used Lumley's definition of coherent structures to derive dynamical models.(45–47) The method has proved to be very successful in describing wall turbulence dynamics. Lumley utilized the proper orthogonal decomposition (POD) theorem of probability theory(44) to represent a realization of a random function as a series of deterministic functions with random coefficients. This is a well-known procedure in signal analysis, where it is often referred to as the "Karhunen Loève decomposition."(36) Lumley introduced this statistical tool (which he generalized to several dimensions) to define coherent structures in turbulence. It also has been recently used by Sirovich and co-workers in a number of problems (see, for instance, Sirovich(62, 63) and references therein). Organized patterns, identified with the deterministic (proper orthogonal) functions, are then mathematically defined. They are, in a statistical sense, the most probable features (since, extracted from statistics, they are common to all realizations). Making the hypothesis of ergodicity and stationarity for a turbulent flow, Aubry *et al.*(4) investigated the time evolultion of the structures by putting the time dependence in the random coefficients that they determined by projecting the Navier–Stokes equations onto these basis functions. This procedure is also discussed by Sirovich(62) for its application to turbulence in the case of ergodicity.

The object of this paper is to propose a systematic mathematical tool to study space-time evolution of a complex system. The method consists in a *biorthogonal decomposition* into spatial orthogonal modes (called topos) and temporal orthogonal modes (called chronos). There is no restriction on the dimension of the topos, which can be one-, two-, or three-dimensional. In the 2D and 3D cases, topos should be closely related to certain kinds of physically coherent structures. Although our approach can be viewed as a time-space-symmetric version of the Karhunen–Loève expansion, it is in principle fundamentally different. Only its time-space symmetry can justify the access to the deterministic dynamics and structures without any particular assumption regarding ergodicity of the system, its stationarity, or the uncorrelation of the time points at which data are recorded. This is thus a completely *deterministic* tool (rather than statistical), which can be applied to a laminar, transitional (in particular intermittent), or fully developed turbulent signal. From this viewpoint, we keep in mind that the signal is produced by the dynamics in some phase space. Pursuing this further, we use the biorthogonal decomposition into topos and chronos to be able to analyze the phase space structure of the dynamics. Each spatial mode can be associated with an instantaneous coherent structure which has a temporal evolution directly given by its corresponding temporal mode. This should address the criticism by Wallace and Hussain(70) on current available tools to study coherent structures: "It is not enough to know the most probable distributions of vorticity or velocity fluctuations. It is necessary to know how the patterns will evolve."

The paper is organized as follows. In Section 1, we show the existence of a spatiotemporal decomposition of a signal into spatial and temporal orthogonal modes which are coupled (in the sense that there is a one-to-one correspondence). We then define in Section 2 global characteristics of the signal: a dimension, three energies, and entropies. Attention is particularly given to the robustness of the dimension in cases where time and/or space are discretized. In Section 3, we establish the connection between the decomposition and the underlying dynamical system. These ideas are finally applied to a coupled map lattice which displays spatiotemporal intermittency in Section 4 and to experimental data in a transitional flow on a rotating flat disk in Section 5.

1. A SPATIOTEMPORAL BIORTHOGONAL DECOMPOSITION

We first consider the analysis of a space-time signal obtained by simultaneous measurements at multiple locations in the flow domain over a sufficiently long time. While this may not be a problem for flows numerically simulated (although a sufficiently long integration time for fully developed flows is often costly), this is a hard task for experimentalists who have to overcome the difficulty of probe interference in the case of hot wires and hot films and a high cost in the case of laser-Doppler anemometry. In certain flows, however, simultaneous measurements with a rake of hot wires are possible (see, e.g., Glauser *et al.*(26)). Some more efficient experimental techniques have been designed, such as the laser scanning technique used, for example, by Ciliberto *et al.*,(18) the image processing of hydrogen bubble lines used by Smith and Paxton(64) in the turbulent boundary layer (and also by Fincham and Blackwelder(24)), and the particle image velocimetry (PIV) (see, e.g., Adrian(2) and Khalighi(39)). In the latter, multiple exposure image of light from small particles moving with the fluid is analyzed to obtain the particle displacements and hence the fluid velocity at many spatial locations. All these image processing techniques have experienced rapid expansion in the last few years. For the reverse operation in which we seek to recover the signal, we will see that the necessary data are the spatial two-point correlation (defined with a temporal measure) and its equivalent, the temporal two-point correlations (defined with a spatial measure).

In this section, we are considering the analysis of a deterministic space-time signal $u(x, t)$ which is the result of simultaneous measurements at different spatial locations over a certain time. We call the signal u by analogy with the velocity, but of course it can be any other variable, such as the pressure, the vorticity, etc. In the following, X denotes the set of spatial measurement points and T the set of times at which measurements are recorded. We can consider either $X = R^n$ or $X = Z^n$ or subsets of one of these. In the same way, we can consider either $T = R$ or $T = Z$ or subsets of R or Z. In particular, if $n = 2$, the measurements are two-dimensional (2D) and we are seeking for 2D flow structures; if $n = 3$, the measurements are three-dimensional (3D) and will represent 3D flow structures.

Definition 1.0. A signal is a measurable, complex-valued function u defined on $X \times T$. At first, we will consider a scalar function $u \in R$. The analysis will be generalized to a vectorial signal $u \in R^d$ in Theorem 1.13. The signal can be a continuous function $u \in C(X \times T)$, a square-integrable function $u \in L^2(X \times T)$, a bounded function $u \in L(X \times T)$, or, by extension, a tempered distribution $u \in S(X \times T)$.

Proposition 1.1. Each signal defines a linear operator

$$U: \quad L^2(X) \to L^2(T)$$

such that

$$\forall \varphi \in L^2(X), \qquad (U\varphi)(t) = \int_X u(x, t)\, \varphi(x)\, dx \tag{1.1}$$

The adjoint operator is defined as

$$U^*: \quad L^2(T) \to L^2(X)$$

such that

$$\forall \psi \in L^2(T), \qquad (U^*\psi)(x) = \int_T \overline{u(x, t)}\, \psi(t)\, dt \tag{1.2}$$

where the bar denotes the complex conjugate.

Proposition 1.2. Formulas (1.1) and (1.2) define bounded operators in the case where $u \in L^2(X \times T)$, for instance. In the other cases, the operators U and U^* can still be defined on appropriate restricted domains $D(U)$ in $L^2(X)$ and $D(U^*)$ in $L^2(T)$.(37)

Proposition 1.3. The analysis of the signal $u(x, t)$ is reduced to the spectral analysis of the operator U. The existence of a continuous part in the spectrum is possible. However, if $u \in L^2(X \times T)$ or if X and T are compact and u is a continuous function $u \in C(X \times T)$, then U is a compact operator and the spectrum of U consists of a denumerable set of isolated, singular points. In the following, we will suppose that the operator U is indeed compact (and so is U^*). As an example of this, we assume that $u \in L^2(X \times T)$.

Proposition 1.4. We now introduce the operators:

$$R: \quad L^2(T) \to L^2(T)$$

such that

$$R = UU^*$$

and

$$L: \quad L^2(X) \to L^2(X)$$

such that

$$L = U^*U$$

The operator R is the integral, nonnegative operator whose kernel is the temporal correlation of the signal $u(x, t)$. Similarly, the operator L is the integral, nonnegative operator whose kernel is the temporal two-point correlation of the signal $u(x, t)$.

Proof. Let us consider a function ψ in $L^2(T)$. We can write

$$\begin{aligned}(R\psi)(t) &= (UU^*\psi)(t)\\ &= \int_X u(x, t)(U^*\psi)(x)\, dx\\ &= \int_X \int_T u(x, t)\, \overline{u(x, s)}\, \psi(s)\, dx\, ds\\ &= \int_T r(t, s)\, \psi(s)\, ds\end{aligned}$$

where $r(t, s)$ is the temporal correlation function of the signal $u(x, t)$ defined as the following:

$$r(t, s) = \int_X u(x, t)\, \overline{u(x, s)}\, dx \tag{1.3}$$

The proof relative to the operator $L = U^*U$ is identical to the previous one where space and time variables must simply be interchanged, the spatial correlation function of the signal $u(x, t)$ being defined as

$$l(x, y) = \int_T u(x, t)\, \overline{u(y, t)}\, dt \tag{1.4}$$

Theorem 1.5. This is the theorem of the analysis of the signal $u(x, t)$. There exists a canonical decomposition of the signal $u(x, t)$ such that

$$u(x, t) = \sum_{k=1}^{\infty} \alpha_k \overline{\varphi_k(x)}\, \psi_k(t) \tag{1.5}$$

with

$$\alpha_1 \geqslant \alpha_2 \geqslant \cdots > 0$$

$$\lim_{N \to \infty} \alpha_N = 0$$

$$(\varphi_k, \varphi_l) = (\psi_k, \psi_l) = \delta_{k,l}$$

The series (1.5) converges in norm.

Definition 1.6. We call "topos" the elements of the orthonormal sequence $\{\varphi_k\}$ in $L^2(X)$ (spatial modes) and "chronos" those of the sequence $\{\psi_k\}$ in $L^2(T)$ (temporal modes).

Proof of Theorem 1.5. (This is a classical demonstration in the theory of functional analysis of operators; see, for example, Kato[(37)]). Since $L = U^*U$ is a nonnegative operator, compact in $L^2(X)$, it has nonnegative eigenvalues and its spectral decomposition can be written in the form

$$L = U^*U = \sum_{k=1}^{\infty} \alpha_k^2(\cdot, \varphi_k)\varphi_k \tag{1.6}$$

where the functions φ_k are orthonormal:

$$(\varphi_k, \varphi_l) = \delta_{k,l}.$$

[The parentheses refer to the scalar product in $L^2(X)$.]

It immediately follows that the functions φ_k are the eigenfunctions of the operator $L = U^*U$ associated with the eigenvalues α_k^2:

$$L\varphi_k = U^*U\varphi_k = \alpha_k^2\varphi_k \qquad \text{with} \quad \alpha_1 \geqslant \alpha_2 \geqslant \cdots > 0 \tag{1.7}$$

If we introduce the set of functions

$$\psi_k = \alpha_k^{-1} U\varphi_k \tag{1.8}$$

it is trivial to show that the functions ψ_k are orthonormal in $L^2(T)$:

$$\begin{aligned}(\psi_k, \psi_l) &= \alpha_k^{-1}\alpha_l^{-1}(U\varphi_k, U\varphi_l)\\ &= \alpha_k^{-1}\alpha_l^{-1}(U^*U\varphi_k, \varphi_l)\\ &= \alpha_k\alpha_l^{-1}(\varphi_k, \varphi_l)\\ &= \delta_{k,l}\end{aligned}$$

Let us now show that

$$U = \sum_{k=1}^{\infty} \alpha_k(\cdot, \varphi_k)\psi_k \tag{1.9}$$

Since the functions $\{\varphi_k\}$ are orthonormal as well as the functions $\{\psi_k\}$ and the eigenvalue series α_k^2 tends to zero as k tends to infinity, the series in the right-hand side of (1.9) converges in norm and it suffices to show that its sum is equal to the operator U for a total set of vectors in $L^2(X)$, that is, a set of functions whose linear combinations are dense in $L^2(X)$. We can choose such a total set $\{\varphi'_k\}$ as the set of the functions $\{\varphi_k\}$ to which we add an orthonormal basis $\{\varphi'_l\}$ of $\operatorname{Ker}(U) = \{\varphi \in L^2(X),\ U\varphi = 0\}$. Equation (1.9) can then be easily shown, using the definition (1.8) of the functions ψ_k and the following orthogonality:

$$\forall k, j \quad (\varphi_k, \varphi'_j) = 0$$

Finally, Theorem 1.5 is simply the result of a kernel identification since, on the one hand, we have

$$\begin{aligned}(U\varphi)(t) &= \sum_{k=1}^{\infty} \alpha_k(\varphi, \varphi_k)\, \varphi_k(t)\\ &= \int_X \left[\sum_{k=1}^{\infty} \alpha_k \overline{\varphi_k(x)}\, \psi_k(t)\right] \varphi(x)\, dx\end{aligned}$$

and on the other hand, we can use the definition of the operator U (see Section 1.1). In the following, we will refer to (1.5) as the "biorthogonal decomposition."

Remark that if U is not compact, and in particular if it has a continuous component in the spectrum, an analogous spectral analysis can, in principle, also be performed, but it is much more difficult to realize in practice. However, in special situations, it is a usual tool as it is indeed the case for a homogeneous or stationary signal for which the Fourier spectrum coincides with the spectral decomposition of the operator U. The notion of discrete topos and chronos can only be recovered in an approximation sense using the Weyl criterion, namely that for $\varepsilon > 0$ and for α in the spectrum of U, there is a (quasi) topo φ_ε and a (quasi) chrono ψ_ε such that

$$\|U^* U\varphi_\varepsilon - \alpha^2 \varphi_\varepsilon\| < \varepsilon$$

and

$$\|UU^* \psi_\varepsilon - \alpha^2 \psi_\varepsilon\| < \varepsilon$$

Proposition 1.7. It is trivial to check that the functions ψ_k introduced in (1.8) are eigenfunctions of the operator $R = UU^*$ associated with the eigenvalues α_k^2:

$$R\psi_k = UU^* \psi_k = \alpha_k^2 \psi_k \tag{1.10}$$

Remark 1.8. When some eigenvalues α_k^2 are degenerate, the associated normalized eigenfunctions are not unique, nor is the decomposition of the signal as stated in Theorem 1.5. This, however, is not a major difficulty, since the subspace associated with each eigenvalue is unique and has a finite dimension.

Remark 1.9. The decomposition (1.5) of the signal $u(x, t)$ can be obtained similarly if the operator U is defined as U: $L^2(T) \to L^2(X)$ in (1.1). This has important consequences on the efficiency of the numerical computation of the eigenfunctions $\{\varphi_k\}$ and $\{\psi_k\}$, as we will see in Sections 5 and 6.

Remark 1.10. There has been some criticism, reported, for example, by Lumley,$^{(48)}$ that decompositions of the type of (1.5) may be restrictive due to the fact that they exclusively use two-point correlations. A trivial generalization of Proposition 1.4 together with Proposition 1.7 shows that this is not true. The biorthogonal decomposition includes (space/time) correlations of higher order as well. This comes from the fact that, in our framework, these (higher order) correlations correspond to various products of the operator U and the operator U^* (in a compatible way). For instance, the kernel of the operator UU^*U is

$$r_3(t/x, s|y) = \int_X \int_T u(x, t)\, \overline{u(x, s)}\, u(y, s)\, dx\, ds \tag{1.11}$$

Now the eigenvectors, in the sense of Theorem 1.5, of such products are clearly the topos and chronos defined above. Only the eigenvalues change.

Proposition 1.11. Since U: $L^2(X) \to L^2(T)$ is a bounded, linear operator, there exists a positive operator V: $L^2(X) \to L^2(X)$ and a partial isometry G: $L^2(X) \to L^2(T)$ such that U can be decomposed in the form

$$U = GV \tag{1.12}$$

This is the polar decomposition of U. While the positive operator V, also defined as

$$V = (U^*U)^{1/2} \tag{1.13}$$

can be expressed from (1.9) in terms of the eigenvalues and the topos

$$V = \sum_{k=1}^{\infty} \alpha_k(\cdot, \varphi_k)\varphi_k \tag{1.14}$$

the partial isometry G is defined by

$$G\varphi_k = \psi_k \qquad \text{and} \qquad \forall \varphi \in \mathrm{Ker}(U), \quad G\varphi = 0 \tag{1.15}$$

The polar decomposition of the adjoint operator U^* can be obtained similarly:

$$U^* = G^*W$$

with

$$W = \sum_{k=1}^{\infty} \alpha_k(\cdot, \psi_k)\psi_k \tag{1.16}$$

It is interesting to note that V is an integral operator whose kernel

$$v(x, x') = \sum_{k=1}^{\infty} \alpha_k \varphi_k(x)\overline{\varphi_k(x')} \tag{1.17}$$

can be considered as the correlation function of a purely spatial signal for which the "statistics" is given by the indices k of the eigenvalues and the eigenmodes. The (spatial) statistical signal takes the form

$$\hat{v}_k(x) = \sqrt{\alpha_k}\, \varphi_k(x) \tag{1.18}$$

Similarly, we can define a temporal "statistical" signal

$$\hat{w}_k(t) = \sqrt{\alpha_k}\, \psi_k(t) \tag{1.19}$$

whose correlation is the kernel of W, given explicitly by

$$w(t, t') = \sum_{k=1}^{\infty} \alpha_k \psi_k(t) \overline{\psi_k(t')} \tag{1.20}$$

It is remarkable to notice that although Theorem 1.5' leads to a spatiotemporal decomposition of the signal in which spatial and temporal modes are intrinsically coupled (they have the same eigenvalues), it is also possible to separate the spatial and temporal information by the method exposed here. We thus recover uniquely spatial structures of the flow $\hat{v}_k(x)$ (perhaps the eddies effectively observed) and uniquely temporal structures $\hat{w}_k(t)$. In the following, we will refer to the product $\hat{v}_k(x)\,\hat{w}_k(t)$ as a (spatiotemporal) "structure." It represents one term in the biorthogonal decomposition (1.5).

Theorem 1.12. We now rewrite (1.9) in the following way:

$$U = \sum_{k=1}^{n} \alpha_k(\cdot, \varphi_k)\psi_k + \sum_{k=n+1}^{\infty} \alpha_k(\cdot, \varphi_k)\psi_k \tag{1.21}$$

The norm of the second term, which can be considered as the error in a Galerkin approximation, is smaller than the smallest eigenvalue of the first term.

Proof. For all integer p, we can write

$$\begin{aligned} \left\| \sum_{k=n+1}^{p} \alpha_k(\varphi, \varphi_k)\psi_k \right\|^2 &= \sum_{k=n+1}^{p} \alpha_k^2 |(\varphi, \varphi_k)| \\ &\leqslant \alpha_{n+1}^2 \sum_{k=n+1}^{p} (\varphi, \varphi_k)| \\ &\leqslant \alpha_{n+1}^2 \|\varphi\|^2 \end{aligned}$$

and thus

$$\left\| \sum_{k=n+1}^{\infty} \alpha_k(\cdot, \varphi_k)\psi_k \right\| \leqslant \alpha_{n+1} \qquad \text{with} \quad \alpha_n \to 0 \text{ if } n \to \infty \tag{1.22}$$

This implies that, in a Galerkin approximation where U is replaced by the truncated sum

$$U_n = \sum_{k=1}^{n} \alpha_k(\cdot, \varphi_k)\psi_k \tag{1.23}$$

the error is smaller than the first neglected eigenvalue α_{n+1}.

Theorem 1.13. If the signal is in $L^1(X \times T)$, a decomposition of the temporally centered signal is given by the biorthogonal decomposition of the original signal with temporally centered chronos suitably renormalized. Similarly, a decomposition of the spatially centered signal is given by the biorthogonal decomposition of the original signal with spatially centered topos also suitably renormalized.

Remark that since $\langle U \rangle_t$ and $\langle U \rangle_x$ are constant operators, they are bounded if T and X are of bounded measure. In a more general context, they can be considered as unbounded operators (with a dense domain).

This has important consequences in turbulence in which a Reynolds decomposition is often applied. When this is the case, the signal is decomposed into a mean and a "fluctuation" and one is interested in decomposing the fluctuation only. Structures of the fluctuation are often called "coherent structures" by the turbulence community; these are the characteristic structures of the turbulent flow, once the mean has been extracted. In shear flow turbulence (in which there is a nonzero mean velocity gradient), big eddies (the largest structures of the fluctuating flow field) extract their energy from the mean flow and transfer it to smaller eddies or finer structures. When the average is a temporal average (as in most experiments), the signal is temporally centered; when the average is a spatial average (as in most numerical simulations), the signal is spatially centered. In homogeneous, stationary turbulence, a hypothesis of ergodicity is applied (twice) and these two averages are assumed to be identical. This, however, is not a general situation and is not assumed in our case.

Proof. We define the spatial average of φ as

$$\forall \varphi \in L^1(X), \qquad E_x(\varphi) = \int_X \varphi(x)\, dx \tag{1.24}$$

and the temporal average of ψ as

$$\forall \psi \in L^1(T), \qquad E_t(\psi) = \int_T \psi(t)\, dt \tag{1.25}$$

Similarly, we define a temporal average of the signal $u(x, t)$,

$$\langle u \rangle_t(x) = \int_T u(x, t)\, dt \tag{1.26}$$

We now consider the time-averaged operator

$$\langle U \rangle_t\colon \ L^2(X) \to L^2(T)$$

such that

$$(\langle U\rangle_t\varphi)(t)=\int_X \langle u\rangle_t(x)\,\varphi(x)\,dx \tag{1.27}$$

which is a constant operator. We then have

$$E_t(\langle U\rangle_t\varphi)=\langle U\rangle_t\varphi \tag{1.28}$$

which leads to the relation

$$\forall\varphi\in L^2(X),\qquad E_t((U-\langle U\rangle_t)\varphi)=0 \tag{1.29}$$

Similarly,

$$\forall\psi\in L^2(T),\qquad E_x((U^*-\langle U^*\rangle_x)\psi)=0 \tag{1.30}$$

Using (1.26) and (1.27) and the biorthogonal decomposition (1.5), we get a decomposition of the temporal average of the operator U:

$$\begin{aligned}\langle U\rangle_t\varphi(t)&=\int_X\int_T u(x,t)\,\varphi(x)\,dx\,dt\\&=\sum_{k=1}^{\infty}\alpha_k(\varphi,\varphi_k)\,E_t(\psi_k)\end{aligned} \tag{1.31}$$

as well as a decomposition of the temporal fluctuation of U:

$$U-\langle U\rangle_t=\sum_{k=1}^{\infty}\alpha_k(\cdot,\varphi_k)[\psi_k-E_t(\psi_k)] \tag{1.32}$$

Similarly, we can write a decomposition of the spatial fluctuation of U:

$$U^*-\langle U^*\rangle_x=\sum_{k=1}^{\infty}\alpha_k(\cdot,\psi_k)[\varphi_k-E_x(\varphi_k)] \tag{1.33}$$

Decompositions of the centered (or fluctuating) signals immediately become

$$u(x,t)-\langle u(x,t)\rangle_t=\sum_{k=1}^{\infty}\alpha_k\overline{\varphi_k(x)}\,[\psi_k(t)-E_t(\psi_k(t))] \tag{1.34}$$

and

$$u(x,t)-\langle u(x,t)\rangle_x=\sum_{k=1}^{\infty}\alpha_k\overline{\varphi_k(x)-E_x(\varphi_k(x))}\,\psi_k(t) \tag{1.35}$$

Finally, since

$$\|\psi_k - E_t(\psi_k)\|^2 = 1 - E_t(\psi_k)^2 \tag{1.36}$$

and similarly

$$\|\varphi_k - E_x(\varphi_k)\|^2 = 1 - E_x(\varphi_k)^2 \tag{1.37}$$

we note that the eigenvalues are multiplied by the factor $[1 - E_t(\psi_k)^2]^{1/2}$ for a temporally centered signal and the factor $[1 - E_x(\varphi_k)^2]^{1/2}$ for a spatially centered signal. A specific case, however, arises when the eigenfunction is equal to its average: this occurs when the mean appears as an eigenfunction which is then a constant. In this case the corresponding eigenvalue is zero, although it was different from zero in the decomposition of the original signal.

Remark 1.14. The decompositions given by Theorem 1.13 for a temporally or spatially centered signal are not biorthogonal, namely the sequence of centered chronos in Eq. (1.34) is not orthogonal in $L^2(T)$ and the sequence of centered topos in Eq. (1.35) is not orthogonal in $L^2(X)$. In other words, decomposition (1.32) does not correspond to the biorthogonal decomposition of the operator $U - \langle U \rangle_t$ and similarly decomposition (1.33) does not coincide with the biorthogonal decomposition of the operator $U - \langle U \rangle_x$. The relation between the biorthogonal decomposition of U and that of $U - \langle U \rangle_x$ (or $U - \langle U \rangle_t$) is rather complex and is not given here. From our viewpoint, indeed it is not natural to center the signal, since each topo and chrono has its own mean: taking the mean of the topos is equivalent to introducing an artificial correlation among them equal to $-E_x(\varphi_k)\,E_x(\varphi_l)$ for all pairs (φ_k, φ_l). Similarly, centering the chronos introduces a correlation $-E_t(\psi_k)\,E_t(\psi_l)$. Note that the use of Fourier analysis has made centering a straightforward and natural operation, since there the mean is simply a component of the decomposition. This is not the case for other expansions, such as the biorthogonal decomposition studied here (except in special cases). Although it is often common practice in turbulence and other fields, a centering operation should thus be carried out carefully with respect to the biorthogonal decomposition.

Proposition 1.15. Let us now suppose that the signal is vectorial. This is indeed often the case in hydrodynamics when the signal is, for example, the velocity, the vorticity, or other vector field such as the 3 components of the velocity and the temperature, etc. Then, we have

$$\forall (x, t) \in X \times T, \qquad \mathbf{u}(x, t) \in R^d \quad \text{with } d = 1, 2, 3,... \tag{1.38}$$

Of course, the case $d=1$ follows the previous analysis. The case $d>1$ requires a slight generalization. For this, we consider the operator

$$U\colon \quad L^2(X, R^d) \to L^2(T)$$

such that

$$\forall \varphi \in L^2(X, R^d), \qquad (U\boldsymbol{\varphi})(t) = \sum_{i=1}^{d} \int_X u_i(x, t)\, \varphi_i(x)\, dx \tag{1.39}$$

where a_i denotes the ith component of the vector $\mathbf{a}$.

The generalization is straightforward if one uses the canonical scalar product in $L^2(X, R^d)$:

$$(\boldsymbol{\varphi}, \boldsymbol{\zeta}) = \sum_{i=1}^{d} \int_X \varphi_i(x)\, \overline{\zeta_i(x)}\, dx \tag{1.40}$$

for which we could have also used tensor notation.

As in Proposition 1.1, we can define the conjugate operator U^*:

$$U^*\colon \quad L^2(T) \to L^2(X, R^d)$$

such that

$$\forall \psi \in L^2(T), \qquad (U^*\psi)_i(x) = \int_T \overline{u_i(x, t)}\, \psi(t)\, dt \tag{1.41}$$

It is trivial to show, using (1.23) and (1.24), that U^* is the adjoint operator of U, i.e.,

$$(\psi, U\boldsymbol{\varphi}) = (U^*\psi, \boldsymbol{\varphi}) \tag{1.42}$$

As in Proposition 1.4, the operator $R = UU^*$ defined in $L^2(T)$ is an integral operator whose kernel is the temporal correlation of the signal (the proof is similar to that given in Proposition 1.4) and the operator $L = U^*U$ defined in $L^2(X, R^d)$ is the integral operator whose kernel is the (tensorial) spatial correlation of the signal. This can be explicitly written in the following way:

$$\begin{aligned}(U^*U\boldsymbol{\varphi})_j &= \int_T (U\boldsymbol{\varphi})(t)\, \overline{u_j(x, t)}\, dt \\ &= \sum_{i=1}^{d} \int_X \int_T u_i(y, t)\, \overline{u_j(x, t)}\, \varphi_i(y)\, dy\, dt \end{aligned} \tag{1.43}$$

Thus, the element (i, j) of the matrix $[U^*U]_{ij}$ is defined by the kernel

$$\int_T u_i(x, t)\,\overline{u_j(y, t)}\,dt \tag{1.44}$$

which is indeed the spatial two-point correlation of the signal.

Finally, as in Theorem 1.5, we can write the (spatiotemporal) decomposition of the signal:

$$u_i(x, t) = \sum_{k=1}^{\infty} \alpha_k \psi_k(t)\,\overline{\varphi_k^i(x)} \tag{1.45}$$

2. SPACE-TIME CHARACTERISTICS OF THE SIGNAL

As is well known, chaos is characterized by sensitivity to initial conditions and a fractal structure. Quantification of these properties for temporal strange attractors has been achieved by determining the fractal dimension of the attractor, its entropy (or degree of chaos), and the Liapunov exponents, which give information on the local stability of the attractor. There are, however, different ways to approximate the dimension(29,35) and to define the entropy (for instance, Kolmogorov–Sinai entropy). The connection between the various definitions is not quite clear yet.

We propose to relate the properties of the spatiotemporal regular and chaotic behavior of the system and its various transitions with quantities extracted from biorthogonal decomposition (1.5). Characteristic quantities of a given signal are of three types: energies, entropies, and dimension. Since the signal carries both spatial and temporal information, global functions which are representative of space and time are introduced. We also define an energy and an entropy which are only temporal or spatial. The dimension, however, is necessarily a global quantity.

Since this biorthogonal expansion (1.5) is valid for a deterministic signal of any kind, ordered or disordered, laminar or turbulent, the following description of the signal can be applied to a nonchaotic or chaotic state. This is particularly appropriate to the study of transition and fully turbulent flows which undergo various instabilities.

2.1. SIGNAL ENERGIES

2.1.1. Global Energy

Proposition 2.1. The global energy of the signal given by the square of the norm of the signal in $L^2(X \times T)$ is equal to the sum of the eigenvalues of decomposition (1.5):

$$E(u) = \int_X \int_T u(x, t)\,\overline{u(x, t)}\,dx\,dt = \sum_{k=1}^{\infty} \alpha_k^2 \tag{2.1}$$

It follows that the energy of a structure is simply given by its eigenvalue. Note that $E(u)$ can be expressed in terms of the operator U and its adjoint: $E(u) = \mathrm{Tr}(U^*U) = \mathrm{Tr}(UU^*)$.

Proof. The derivation of (2.1) is straightforward from decomposition (1.5) and the orthogonality of the topos and that of the chronos.

Note that if the signal is the velocity field, the energy becomes the kinetic energy of the flow (in a generalized sense, since the flow is not necessarily statistically stationary), which is also the sum of the eigenvalues:

$$E(\mathbf{u}) = \sum_{i=1}^{3} \int_X \int_T u_i(x, t)\, \overline{u_i(x, t)}\, dx\, dt = \sum_{k=1}^{\infty} \alpha_k^2 \tag{2.2}$$

Again, $E(\mathbf{u})$ can be expressed in terms of the operator U and its adjoint: $E(\mathbf{u}) = \mathrm{Tr}(U^*U) = \mathrm{Tr}(UU^*)$. Space-time structures participate independently in the kinetic energy of the flow.$^{(45-47)}$ This is completely consistent with the classical conception of turbulence in which eddies of different sizes contain a certain amount of kinetic energy (see, for example, Kolmogorov$^{(41)}$ for a description of isotropic, homogeneous turbulence).

2.1.2. Spatial Energy

Definition 2.2. The spatial energy of the signal which evolves in time is

$$\int_X u(x, t)\, \overline{u(x, t)}\, dx = \sum_{k=1}^{\infty} \alpha_k^2 |\psi_k(t)|^2 \tag{2.3}$$

The proof is similar to that of the previous proposition. This time-dependent function, in which the spatial information of the signal has been integrated, should be useful to study temporal intermittency as it occurs in many transition and turbulent flows, the most characteristic one perhaps being the bursting event near a wall.

2.1.3. Temporal Energy

Definition 2.3. In the same way in which we introduced a spatial energy, we now define a temporal energy of the signal which spatially evolves:

$$\int_T u(x, t)\, \overline{u(x, t)}\, dt = \sum_{k=1}^{\infty} \alpha_k^2 |\varphi_k(x)|^2 \tag{2.4}$$

This definition should be characteristic of the (temporal) energetic content of the signal and its spatial distribution. The different regions of the flow can then be classified on an energy criterion.

2.1.4. Robustness of the Global Energy for a Discretized Signal.

We now investigate the robustness of the notion of global energy when the sets X and (or) T (as defined in Section 1) consist(s) of a finite number of points, as is often the case for experimental or numerical signals. More specifically, the question is how the addition of one point in X or T affects the global energy of the signal. Note that the extra point can be inserted either in between the original points or at the beginning or at the end of the series.

Here, the original signal $u(x, t)$ is defined in the discretized sets X and T, which can be explicitly written as $X = \{x_1, x_2, \dots, x_n\}$ and $T = \{t_1, t_2, \dots, t_m\}$.

Let us now consider the new set:

$$X' = X \cup \{x_{n+1}\} \tag{2.5}$$

if we add a spatial location, or

$$T' = T \cup \{t_{m+1}\} \tag{2.6}$$

if we add a point in time.

In the following, we assume that we add a spatial point, so that the new signal $\hat{u}(x, t)$ is a function of $L^2(\hat{X} \times \hat{T})$ such that $\hat{X} = X'$ and $\hat{T} = T$. Since there is complete space-time symmetry, the analysis is the same if one point in time is added instead, in which case we have $\hat{X} = X$ and $\hat{T} = T'$. The new signal $\hat{u}$ satisfies

$$\forall t, \forall x \in X, \qquad \hat{u}(x, t) = u(x, t) \tag{2.7}$$

and the values $\hat{u}(x_{n+1}, t)$ at the extra point are determined by the extra measurements.

Proposition 2.4. The new signal energy $E(\hat{u})$ satisfies

$$E(u) + \hat{\alpha}_{d+1}^2 \leqslant E(\hat{u}) \leqslant \hat{\alpha}_1^2 + E(u) \tag{2.8}$$

where $E(u)$ is the global energy of the signal u and $\hat{\alpha}_1^2$ and $\hat{\alpha}_{d+1}^2$ are the first and last nonzero eigenvalues in the decomposition of the new signal.

Proof. Relation (2.7) between the original and the new signal implies

$$\forall i, j \leqslant n, \qquad \hat{a}_{ij} = a_{ij} \tag{2.9}$$

where $A = \{a_{ij}\}$ denotes the $n \times n$ matrix U^*U and $\hat{A} = \{\hat{a}_{ij}\}$ the $(n+1) \times (n+1)$ matrix $\hat{U}^*\hat{U}$. The (global) energy of the original signal and the new signal are the traces of the matrices A and $\hat{A}$, respectively.

Using the Courant minimax theorem, we can obtain order relations between the eigenvalues $\alpha_k^2 = \lambda_k$ of A and $\hat{\alpha}_k^2 = \hat{\lambda}_k$ of $\hat{A}$ (all being counted with their multiplicity):

$$\hat{\lambda}_1 \geqslant \lambda_1 \geqslant \hat{\lambda}_2 \geqslant \lambda_2 \geqslant \cdots \geqslant \hat{\lambda}_n \geqslant \lambda_n \geqslant \hat{\lambda}_{n+1} \tag{2.10}$$

if d is the number of nonzero eigenvalues of the matrix A, then

$$\lambda_d \neq 0 \qquad \text{and} \qquad \forall k \geqslant d+1, \quad \lambda_k = 0 \tag{2.11}$$

and consequently, using (2.10),

$$\hat{\lambda}_d \neq 0 \qquad \text{and} \qquad \forall k \geqslant d+2, \quad \hat{\lambda}_k = 0 \tag{2.12}$$

Combining (2.10) and (2. 12), we get

$$\sum_{k=2}^{d+1} \hat{\lambda}_k \leqslant \mathrm{Tr}(A) \leqslant \sum_{k=1}^{d} \hat{\lambda}_k \tag{2.13}$$

where

$$\mathrm{Tr}(A) = \sum_{k=1}^{d} \lambda_k \tag{2.14}$$

It then immediately follows that

$$\mathrm{Tr}(A) + \hat{\lambda}_{d+1} \leqslant \mathrm{Tr}(\hat{A}) \leqslant \hat{\lambda}_1 + \mathrm{Tr}(A) \tag{2.15}$$

or equivalently

$$E(u) + \hat{\lambda}_{d+1} \leqslant E(\hat{u}) \leqslant \hat{\lambda}_1 + E(u)$$

as previously stated.

2.2. Signal Entropies

Another characteristic parameter of the signal is its degree of order or disorder. It is then natural to define the corresponding entropy. As for the energy, we define a global, a temporal, and a spatial entropy.

2.2.1. Global Entropy

We first define a global quantity characterizing the full space-time structure of the signal.

Definition 2.5. Letting the normalized or relative energy of each structure be

$$p_k = \alpha_k^2 \Big/ \sum_{k=1}^{\infty} \alpha_k^2 \tag{2.16}$$

the expression of the global entropy of the space-time signal is

$$H(u) = -\lim_{N\to\infty} \frac{1}{\log N} \sum_{k=1}^{N} p_k \log p_k \tag{2.17}$$

We introduce the normalizing factor $(\log N)^{-1}$ in order to perform comparisons between different signal entropies. $H(u)$ is zero if and only if only one eigenvalue is nonzero, i.e., all the signal energy is concentrated in the first structure. As usual, in the opposite case, if all the eigenvalues are equal, i.e., the energy is equidistributed among the structures, then $H(u)$ takes its maximum value, namely 1. At intermediate states, $H(u)$ keeps increasing as the energy spreads out uniformly on the eigenvalues. This function will be useful in hydrodynamics for a quantitative description of the increasing degree of complexity as the Reynolds number (or another dimensionless parameter characteristic of the system such as the Rayleigh number or an aspect ratio) gets higher and higher and the flow evolves toward a fully developed turbulent state and even beyond.

2.2.2. Spatial Entropy

We define a spatial entropy representative of the degree of order of the spatial component of the signal, which of course evolves in time.

Definition 2.6. Letting

$$p_k(t) = \alpha_k |\psi_k(t)| \Big/ \sum_{k=1}^{\infty} \alpha_k |\psi_k(t)| \tag{2.18}$$

the spatial entropy is

$$I(t) = -\lim_{N\to\infty} \frac{1}{\log N} \sum_{k=1}^{N} p_k(t) \log p_k(t) \tag{2.19}$$

As the spatial energy, this function should be particularly interesting in strongly intermittent events in which complex behavior alternates with more regular periods.

2.2.3. Temporal Entropy

We define a temporal entropy of the signal which represents the degree of order of the spatial component of the signal, which of course changes from point to point in space.

Definition 2.7. Letting

$$p_k^*(x) = \alpha_k |\varphi_k(x)| \Big/ \sum_{k=1}^{\infty} \alpha_k |\varphi_k(x)| \tag{2.20}$$

the temporal entropy is

$$I^*(x) = -\lim_{N\to\infty} \frac{1}{\log N} \sum_{k=1}^{N} p_k^*(x) \log p_k^*(x) \tag{2.21}$$

This definition should be useful to evaluate the distribution of "disorder" in the various flow domains.

2.3. Dimension of the Signal

2.3.1. Connection with the Number of Structures

Proposition 2.8. The operator U (corresponding to the signal u) realizes an isomorphism between

$$\chi(X) = \overline{\operatorname{Ran}(U^*)} \subset L^2(X) \tag{2.22}$$

and

$$\chi(T) = \overline{\operatorname{Ran}(U)} \subset L^2(T) \tag{2.23}$$

where $\overline{\operatorname{Ran}(U)}$ and $\overline{\operatorname{Ran}(U^*)}$ denote the closure of $\operatorname{Ran}(U)$ and $\operatorname{Ran}(U^*)$, respectively.

Definition 2.9. We then define the characteristic dimension of the signal, $\dim(u)$, as the common dimension of $\chi(X)$ and $\chi(T)$.

Proof of Proposition 2.8. Again, this is a classical piece of linear analysis.(37) Let us first remark, for further use, that if we write

$$\operatorname{Ker}(U) = \{\varphi \in L^2(X),\ U\varphi = 0\} \tag{2.24}$$

so that

$$\chi(X) = \operatorname{Ker}(U)^\perp \tag{2.25}$$

then we get

$$\chi(X)^\perp = \operatorname{Ker}(U^*U) = \operatorname{Ran}(U^*)^\perp = \operatorname{Ran}(U^*U)^\perp \tag{2.26}$$

and similarly

$$\chi(T)^\perp = \operatorname{Ker}(UU^*) = \operatorname{Ran}(U)^\perp = \operatorname{Ran}(UU^*)^\perp \tag{2.27}$$

It immediately follows that

$$L^2(X) = \operatorname{Ker}(U) \oplus \chi(X) \tag{2.28}$$

and

$$L^2(T) = \mathrm{Ker}(U^*) \oplus \chi(T) \tag{2.29}$$

Finally, we can write the straightforward relations between $\chi(X)$ and $\chi(T)$:

$$\begin{aligned} U\chi(X) &= \chi(T) \\ U^*\chi(T) &= \chi(X) \end{aligned} \tag{2.30}$$

and we will see in more detail in Section 3 that $\dim(u)$ is indeed the number of degrees of freedom of the signal $u(x, t)$.

2.3.2. Robustness of the Dimension for a Discretized Signal

Here we turn to the question of the robustness of the dimension of the signal when X and (or) T are (is) discretized and one point of measurement (in space or time) is added to the signal.

It is clear that the dimensions of $L^2(X)$ and $L^2(T)$ [respectively called $\dim(X)$ and $\dim(T)$] are not necessarily the same. Typically, the number of times is larger than the number of spatial locations in an experiment and vice versa in a numerical simulation of turbulence in which time integrations are costly. In any case, the dimensions have to be sufficiently large so that the signal contains relevant space and time scales. In a fully developed turbulent flow (see, e.g., Tennekes and Lumley[(68)]), the largest scale must be of the order of the most energetic eddies (often called the energy-containing scale or integral scale) and the smallest scale must be as small as the Kolmogorov scale at which energy dissipation occurs (unless one wants to pursue a local study). Letting n and m be $\dim(X)$ and $\dim(T)$, respectively, the number of nonzero eigenvalues (and thus the signal dimension) is necessarily smaller than or equal to the smallest of the two numbers m and n, that is, $\inf(m, n)$. In the case where one of these numbers is much larger than the other one, adding a point to the largest number has no or a minor effect on the dimension.

We use here the notations and hypotheses introduced in Section 2.4. In particular, we assume that the new signal $\hat{u}$ includes one extra spatial point compared with the original signal u and that the number of nonzero eigenvalues is d in the original signal. Then (2.11) and (2.12) imply

$$\lambda_d \neq 0, \qquad \lambda_{d+1} = 0 \tag{2.31}$$

and

$$\hat{\lambda}_d \neq 0, \qquad \hat{\lambda}_{d+2} = 0 \tag{2.32}$$

There is, however, no information concerning $\hat{\lambda}_{d+1}$. This eigenvalue can be zero, in which case the dimension of the new signal $\hat{u}$ equals that of the original signal u:

$$\dim(\hat{u}) = \dim(u), \quad \text{or equivalently} \quad \dim \operatorname{Ker}(A) = \dim \operatorname{Ker}(\hat{A}) - 1 \tag{2.33}$$

Otherwise, the dimension of the new signal will be larger than that of the original signal by one:

$$\dim(\hat{u}) = \dim(u) + 1, \quad \text{or equivalently} \quad \dim \operatorname{Ker}(A) = \dim \operatorname{Ker}(\hat{A}) \tag{2.34}$$

We now completely define the matrix $\hat{U}^*\hat{U} = \hat{A}$, which can be written in terms of the matrix A with an extra row and extra column:

$$\begin{gathered} \forall i \leqslant n, \quad \forall j \leqslant n, \qquad \hat{a}_{ij} = a_{ij} \\ \forall j \leqslant n, \qquad \hat{a}_{n+1,j} = \hat{a}_{j,n+1} = v_j \\ \hat{a}_{n+1,n+1} = a \end{gathered} \tag{2.35}$$

where $\mathbf{v}$ of R^n is the vector consisting of the first n elements of the last column of the matrix $\hat{A}$ and a is the $(n+1)$th element.

These elements are the only part of $\hat{A}$ depending upon the measurement at the new spatial point.

We now show how the case (2.33) is a particular situation.

Proposition 2.10. The addition of one spatial point has no effect on the characteristic dimension if and only if $\mathbf{v} \in \chi(X)$ and $a = (\mathbf{v}, (U^*U)^{-1}\mathbf{v})$, where $(U^*U)^{-1}$ stands for the inverse of the restriction of (U^*U) to $\chi(X)$. The addition of one time step can be treated exact in the same way.

Proof. Let us keep the previous notation: $U^*U = A$ and $\hat{U}^*\hat{U} = \hat{A}$ and consider a vector $\boldsymbol{\eta}$ in $\operatorname{Ker}(\hat{A})$:

$$\hat{A}\boldsymbol{\eta} = 0 \tag{2.36}$$

Letting the element of R^n whose components are the first n components of $\boldsymbol{\eta}$ be the vector $\boldsymbol{\xi}$ and the last component of $\boldsymbol{\eta}$ be x ($x = \eta_{n+1}$), Eq. (2.36) can be written in the form of one vectorial and one scalar equation:

$$\begin{gathered} A\boldsymbol{\xi} + x\mathbf{v} = 0 \\ (\mathbf{v}, \boldsymbol{\xi}) + ax = 0 \end{gathered} \tag{2.37}$$

Also note that

$$L^2(\hat{X}) = \operatorname{Ker}(A) \oplus \operatorname{Ran}(A) \oplus C \tag{2.38}$$

Now suppose that $\dim(u)=\dim(\hat{u})$. Then, since $\mathrm{Ker}(A)\oplus\{0\}\subset\mathrm{Ker}(\hat{A})$, by (2.36) there exists $\boldsymbol{\eta}\in\mathrm{Ker}(\hat{A})$ such that $\boldsymbol{\eta}=\boldsymbol{\xi}\oplus x$ and $\boldsymbol{\xi}\in\mathrm{Ran}(A)=\chi(X)$. Since $A\boldsymbol{\xi}\neq\mathbf{0}$, we can conclude, using the first equation of (2.37), that $x\neq 0$ and $\mathbf{v}=-(1/x)A\boldsymbol{\xi}$ and therefore $\mathbf{v}\in\chi(X)$. Finally, since by Proposition 2.8 the matrix A is invertible on $\chi(X)$, we have $\boldsymbol{\xi}=-xA^{-1}\mathbf{v}$. The second condition of the proposition immediately follows from the second equation of (2.37).

Conversely, if $\mathbf{v}\in\chi(X)$, we take $x=1$ and define $\boldsymbol{\xi}=-A^{-1}\mathbf{v}$ so that the first equation of (2.37) is satisfied. Since the second one can also be easily checked, we get $\boldsymbol{\eta}=\boldsymbol{\xi}\oplus 1\in\mathrm{Ker}(\hat{A})$ and the proposition follows.

Remark 2.11. If, under the condition of Proposition 2.10, we write

$$\mathbf{v}=\sum_{i=1}^{d}\eta_i\boldsymbol{\varphi}_i \tag{2.39}$$

where the vectors $\boldsymbol{\varphi}_i$ are the topos relative to U—note that in principle $\eta_i\neq v_j$—the remaining condition becomes

$$a=\sum_{i=1}^{d}\frac{\eta_i^2}{\alpha_i^2} \tag{2.40}$$

This shows, as expected, that the condition in the proposition tells us that the new measurement does not introduce any new information.

Finally, we would like to mention that it is possible to introduce a relative dimension defined as

$$\delta_n=\frac{\dim(u)}{n} \tag{2.41}$$

which accounts for the fraction of the effective number of degrees of freedom. Unfortunately, in view of the previous proposition, and since

$$\frac{d}{n+1}<\frac{d}{n}<\frac{d+1}{n+1}$$

the existence of a limit of δ_n as n goes to infinity cannot follow from general properties.

Proposition 2.12. In the case where $\dim(\hat{u})=\dim(u)+1$, the relative energy that is taken by the extra degree of freedom is bounded by

$$p_{d+1}\leqslant\frac{a}{E(\hat{u})} \tag{2.42}$$

where p_k has been defined in (2.16).

Proof. We first notice that

$$\mathrm{Tr}(\hat{A}) = \mathrm{Tr}(A) + a \qquad \text{or} \qquad E(\hat{u}) = E(u) + a \tag{2.43}$$

Then Eq. (2.15) yields

$$a \geqslant \hat{\alpha}_{d+1}^2 \tag{2.44}$$

from which the proposition follows from Proposition 2.4.

Remark 2.13. If we assume that the time mean energy of the signal $\hat{u}$ at x_{n+1}

$$a = \sum_t |u(x_{n+1}, t)|^2 \tag{2.45}$$

is of order of the (time) mean of the energy evaluated at the other points $x_1, x_2, \ldots, x_n$, then the right-hand side of (2.42) is of the order $1/(n+1)$. We can thus conclude that even if the dimension increases by one when one point gets added in X or T, the (normalized) energy supported by this new direction in phase space becomes very small as n increases.

3. DECOMPOSITION AND DYNAMICS

In this section, we establish the connection between the biorthogonal decomposition and the properties of the underlying dynamical system. The following analysis is applicable in the general context of any spatiotemporal signal as was introduced in Sections 1 and 2. We, however, use a terminology where u describes phase space motion (such as the position, velocity, momentum, etc., of a given system) in a time asymptotic regime, that is, after the transient.

3.1. Characteristic Space

At each time point $t \in T$, the signal u defines a function of $x \in X$ defined as

$$\forall x \in X, \qquad \xi_t(x) = u(x, t) \tag{3.1}$$

As time t is running, ξ_t is an orbit of the system which has produced the signal u. Let us suppose that $\xi_t \in L^2(X)$. (It is also possible to handle much more general cases.) In this case, $L^2(X)$ is the phase space of the system. We are going to show that the biorthogonal decomposition permits localization of the dynamics in the phase space in two ways. First, we find a Euclidean subspace $\chi(X) \subset L^2(X)$ with a dimension equal to the characteristic dimension introduced in Section 2, $\dim(u)$, such that the orbit ξ_t never leaves $\chi(X)$. We will also show that $\chi(X)$ is minimal for this property, namely there is no other Euclidean subspace of dimension strictly less than $\dim(u)$ which contains the dynamics. Second, it is possible to find bounded regions of $\chi(X)$ in which the system spends most of the time. In other words, the biorthogonal decomposition permits a description of the dynamics in a (characteristic) subspace of the phase space with a presence density concentrated in a bounded region.

As already initroduced in Eq. (2.25), we take $\chi(X)$ as

$$\chi(X) = \operatorname{Ker}(U)^{\perp} \qquad \text{with} \quad \dim \chi(X) = \dim(u) \tag{3.2}$$

Proposition 3.1. $\chi(X)$ is the closed linear span of the family of vectors $\xi_t \in L^2(X)$.

Proof. Since all topas φ_k belong to $\chi(X)$, Theorem 1.5 implies that $\xi_t \in \chi(X)$ for all t (more precisely, for almost all t with respect to Lebesgue measure if T is a continuum). Conversely, we want to show that $\chi(X) \subset \{\xi_t\}$, where $\{\xi_t\}$ denotes the (closed) linear span of the vectors ξ_t or equivalently that

$$\{\xi_t\}^{\perp} \subset \chi(X)^{\perp} = \operatorname{Ker}(U) \tag{3.3}$$

Let us take $\xi \in L^2(X)$ and $\xi \in \{\xi_t\}^{\perp}$. Then, we can write

$$\begin{aligned}(U\xi)(t) &= \int_X u(x, t)\, \xi(x)\, dx \\ &= (\xi_t, \xi) \\ &= 0\end{aligned} \tag{3.4}$$

Therefore, $\xi \in \operatorname{Ker}(U)$ and the proposition follows. The characteristic space $\chi(X)$ is thus the minimal Euclidean embedding of the dynamics in $L^2(X)$.

Let us now localize the orbit ξ_t inside $\chi(X)$. For a bounded region $V \subset \chi(X)$, it is natural to define the mean time of the presence of ξ_t in V as

$$\tau(V) = \lim_{T \to \infty} \frac{1}{T} \int_0^T \zeta_V(\xi_t)\, dt \tag{3.5}$$

where ζ_V is the characteristic function of V ("characteristic" in the mathematical sense, namely 1 or 0 whether the variable belongs to V or not). This is the normalized measure of Section 2. We are particularly interested in the case where V is a ball of radius r:

$$B_r = \{\xi \in \chi(X) : |\xi| \leqslant r\} \tag{3.6}$$

or a cylinder:

$$C(r; k_1, k_2, \ldots, k_1) = \left\{ \xi \in \chi(X) : \left| \sum_{i=1}^{l} \xi^{k_i} \right| \leqslant r \right\} \tag{3.7}$$

where the ξ^k are the coordinates of ξ with respect to the topos φ_k.

Proposition 3.2. If the signal u is centered (see Section 2), then, for each positive real r, we have

$$\tau(B_r) \geqslant 1 - \frac{1}{r^2} E(u) \tag{3.8}$$

where $E(u)$ is the global energy of Section 2.11.

It then suffices to choose r to localize the orbit with great accuracy.

Proof. The proof is similar to that of the Chebyshev inequality, since $E(u)$ can be viewed from (2.1) as the variance of ξ_t with respect to the measure defined by (3.5).

Remark 3.3. Exactly in the same way, we see that

$$\tau(C(r; k)) \geqslant 1 - \frac{1}{r^2} \alpha_k^2 \tag{3.9}$$

and therefore ξ_t^k defined as

$$\xi_t^k = \alpha_k \psi_k(t) \varphi_k \tag{3.10}$$

remains within some bounded domain for a large part of the time. An even better approximation can be achieved by using the Kolmogorov theorem (see, e.g., Gnedenko(27)), since, from Theorem 1.5, the coordinates ξ_t^k can be considered as a sequence of independent random vectors. Therefore, for every subset of coordinates defined by indices $\{k_1, k_2, \ldots, k_l\}$, we can write

$$\tau(C(r; k_1, k_2, \ldots, k_l)) \geqslant 1 - \frac{1}{r^2} \sum_{k_i} \alpha_{k_i}^2 \tag{3.11}$$

3.2. Spatial Structure

The analysis of the spatial complexity of the system can be undertaken by considering, at each point $x \in X$, the time evolution of the local signal

$$\eta_x \in L^2(T) \tag{3.12}$$

defined in the same way as ξ_t in (3.1). Using the space-time symmetry of Section 2, it is easy to rephrase Proposition 3.1 and 3.2. The equivalent space $\chi(T) \subset L^2(T)$ is then the characteristic space of all (temporal) signals detected at each spatial point. The statement corresponding to Remark 3.3 localizes the sites moving in a coherent way (synchronous to each chrono). The profs are exactly the same as those given above. Notice that the linear dependence in this space of η_x for different $x \in X$ has the usual meaning of mutual correlated motions.

3.3. Asymptotic and Ergodic Properties

If, instead of an isolated space-time signal, we consider different realizations of the flow in an experiment or different initial conditions in a numerical simulation, it is natural to define a statistical signal as $\{u_\omega(x, t)\}$ in which ω is a random event taken in a space Ω. It is clear that we can consider time translations on Ω defined as

$$u_{\tau(\omega)}(x, t) = u_\omega(x, t - \tau), \qquad \tau \in T \tag{3.13}$$

For experimental data, (3.13) simply means a change of initial time and for a dynamical system a change of origin of the time coordinate. It is then natural to suppose that some statistical average (i.e., a probability measure) on Ω is given, and since we are interested in time asymptotic properties, the statistical average must be time invariant. Note that this is in essence different from the situation where the statistical average is directly the time average, because in general the time action (3.13) on Ω is far from being ergodic. In such cases, Ω can be decomposed in invariant, two-by-two disjoint pieces, on which the average measure is indeed ergodic (see, e.g., Cornfeld *et al.*[21]). Since it is clear that all the notions introduced in the previous sections are measurable functions of u_ω, and therefore of $\omega \in \Omega$, they ought to be constant on each ergodic component of Ω if they are considered in a time asymptotic regime (i.e., if $t \to \infty$ is introduced in the definitions of Section 2). Such is the case of the energies, the chronos, and the topos as well as the characteristic dimension and entropy.

Then in the study of a statistical space-time signal, all we need is the control of the deviation from the total average:

$$\tilde{u}_\omega(x, t) = u_\omega(x, t) - \langle u_\omega(x, t) \rangle_\omega \tag{3.14}$$

where the ensemble average $\langle \cdot \rangle_\omega$ is given by the invariant measure on Ω. For instance, the Reynolds average in turbulence can be viewed as such a measure. However, using the convex decomposition of an invariant measure in ergodic components, the analysis can simply be carried out by putting together the different ergodic parts. From a practical point of view, since the ergodic components are not known in general, the signal can be studied by means of all the moments of the distributions relative to each quantity introduced so far. Note that the biorthogonal decomposition $\tilde{u}_\omega(x, t)$ can be viewed as the spectral analysis of U_ω as in Section 1 and since, according to (3.4), we have $\tilde{U}_\omega = U_\omega - \langle U_\omega \rangle_\omega$, all studies can be performed in terms of the well-known perturbation theory of linear operators.

Moreover, it is well known that the dynamics of dissipative dynamical systems may converge to one or more attractors. In many cases (see Babin *et al.*$^{(7)}$ and Témam$^{(67)}$ for examples), there is a maximal (global) finite-dimensional attractor—the largest bounded invariant set—for which the Hausdorff dimension can be estimated. This has been shown for various partial differential equations such as the two-dimensional Navier–Stokes equations and for general vector fields in Hilbert space with a compact invariant subset.$^{(50,51)}$ When there indeed exists an attractor on which lies the signal $u(x, t)$, in certain circumstances (among which ergodicity), it is contained in the characteristic space $\chi(X)$ and therefore its dimension is less than or equal to the characteristic dimension $\dim(u)$ defined in the previous section. Under the same hypotheses, we conjecture that inertial manifolds—that is, finite-dimensional, exponentially attracting, positively invariant Lipschitz manifolds (see, e.g., Foias *et al.*$^{(25)}$)—ought to be contained in $\chi(X)$ and therefore the method can be used as a (flat) inertial manifold approximation.

Remark 3.4. Since Proposition 3.1 provides an embedding of the dynamics of $L^2(X)$ in $\chi(X)$, we may want to compare this embedding with the embedding of attractors from time series.

Recall that it is possible to embed times series obtained from a numerical or experimental scalar signal in a "state" space of finite dimension d_E. This can be done, for instance, by a time delay method. In some cases, d_E can be estimated or at least an upper bound can be found$^{(66)}$ and it turns out that, if the dimension of the underlying attractor is κ, this bound is $2\kappa + 1$. Therefore, in principle, $R^{2\kappa+1}$ which contains the time series delayed vector as an embedding. To be more precise, this result needs the compactness and finite dimensionality of some smooth invariant manifold containing the attractor and, as in our case, κ needs to be understood as the (integer) dimension of this manifold. Comparing Proposition 3.1 and the embedding theorem for time series, we see that the main difference is the following. In our case, we start within a given phase space $[L^2(X)]$, whereas in the other case, the construction of this space has to be performed by finding a "state" space diffeomorphic to a part of the phase space. Therefore, it is possible to connect our result to the embeddings of attractors by searching for general conditions so that $2\kappa + 1$ is indeed an upper bound for $\dim(u)$. However, we would like to stress the fact that the two problems are in essence different and thus this connection can be made only under very special assumptions concerning the relation between phase space and "state" space, the reason being that in our case we deal with linear subspaces of $L^2(X)$ and the morphism between the phase space and the "state" spaces is not necessarily linear. However, if this is indeed the case, then $2\kappa + 1$ is effectively an upper bound for $\dim(u)$. Thus, we get the following bounds for the characteristic dimension:

$$\kappa \leqslant \dim(u) \leqslant 2\kappa + 1 \tag{3.15}$$

In general the (global) attractor may carry different ergodic measures and therefore comparing the properties of the biorthogonal decomposition with the quantities related to such measures such as Kolmogorov–Sinai entropy and Liapunov exponents for example is a hard task. The main difficulty is that, as mentioned earlier, the properties of the biorthogonal decomposition as well as the ergodic invariants strongly depend on the ergodic component of Ω where the initial condition stands. Nevertheless, we can think that the selection of the ergodic component where the computation is carried out (or the experiment takes place) is made by the choice of some initial conditions. This guarantees that the analyzed signal corresponds to an orbit in some ergodic component. In this case, a relation between the ergodic invariants and the biorthogonal decomposition clearly arises.

We now illustrate this relation by showing how it works. If $\lambda_1 \geqslant \lambda_2 \geqslant \cdots \geqslant \lambda_r$ are the Liapunov exponents (relative to an ergodic measure ρ) of an attractor A, then the Liapunov dimension$^{(35,59)}$ is defined by

$$\dim_A = K + \frac{1}{|\lambda_{K+1}|} \sum_{k=1}^{K} \lambda_k \tag{3.16}$$

where K is the number of strictly positive μ_i such that $\mu_i = \sum_{k=1}^{i} \lambda_k$.

The meaning of $\dim_A$ can be easily understood if one plots μ_i as a function of i; $\dim_A$ is then given by the abscissa of the (nontrivial) zero of this function, which is obtained by a linear interpolation between the last positive μ_i and the first negative one. Now, denoting by K_A the smallest integer greater than $\dim_A$, if the latter is not an integer, it is clear that $(K_A - 1)$ is the maximal number of linearly independent vectors in the tangent space such that the volume of the hypercube they define exponentially grows in time. In the same way, K_A is the minimal number of linearly independent vectors defining a volume which exponentially decays. In other words, K_A is the dimension of the (asymptotic) tangent space. If, on the other hand, the dynamics fills densely and smoothly some volume of the characteristic space $\chi(X)$, as it should if the system is chaotic or turbulent, the tangent space of $\chi(X)$, a linear space of dimension $\dim(u)$, is identified with the space just mentioned before and we get the following relation between the characteristic dimension and the Liapunov dimension:

$$\dim(u) = K_A = [\dim_A] + 1 \tag{3.17}$$

where $[\dim_A]$ stands for the integer part of $\dim_A$.

Here, to be more precise, the assumption previously made on the "smoothly filling" dynamics is the same as in Taken's embedding theorem,$^{(66)}$ namely that there is a smooth, invariant, finite-dimensional manifold M which is attractive for the dynamics starting at almost every point outside of M.$^{(52)}$ The remaining assumptions of the embedding theorem tell us that the manifold M needs to be open in $\chi(X)$.

This explains the numerical results of Ciliberto and Nicolaenko$^{(20)}$ in which both dimensions are compared for experimental results on Rayleigh–Bénard convection in annular geometry as well as for numerical data obtained from integration of the Kolmogorov–Spiegel–Sivashinsky equation. They found that both numerically computed dimensions are indeed related by relation (3.17). This relation has also been found by Rodriguez and Sirovich$^{(57)}$ for the Ginzburg–Landau equation either with Neumann or Dirichlet boundary conditions. Notice, however, that in these computations, $\dim(u)$ may be larger than the estimated value due to some threshold introduced in the energy spectrum, but then the energy supported by these directions ought to be very small (roughly of the order of roundoff errors). Accordingly, in view of Remark 3.3, the dynamics will ignore these directions for most of the time. We refrain from going further into other examples since for large dimensions (e.g., the numerical computation of Rayleigh–Bénard convection by Sirovich and Deane$^{(63)}$), the comparison between our formula and numerical calculations requires an enormous amount of computational time in order to get reliable conclusions, since an extrapolation for the Liapunov spectrum cannot give the accuracy necessary to conclude.

Following the same line, it is possible to relate other ergodic invariants with the characteristics of the previous section. Not only can the biorthogonal decomposition be considered as a fast algorithm to compute the Liapunov dimension in the case of a turbulent regime where (3.17) may hold, but also the difference between the characteristic dimension and the Liapunov dimension in the general case, that is,

$$\dim(u) - \dim A \tag{3.18}$$

can be considered as an indicator for the transition to a turbulent regime (in view of the previous discussion).

3.4. Characteristic Dimension and Bifurcations

Bifurcations generically appear when dealing with a system depending on a parameter, such as the Reynolds number in hydrodynamics or the coupling coefficient for CML. They correspond to situations where some properties of the dynamics suddenly change. We pass in review some of the most popular bifurcations (see, e.g., Guckenheimer and Holmes(32)) in order to present the corresponding behavior of the biorthogonal decomposition in each case. This behavior, on the other hand, can be used in practical examples as a tool of identification of different types of bifurcations in cases where the complexity of the signal does not allow an easy interpretation as in experiments or a dynamical system with a phase space of large dimension.

We first distinguish, from our point of view, two types of bifurcation: *internal* bifurcations, through which the characteristic dimension $\dim(u)$ does not change, and *external* bifurcations, through which it does change. Internal bifurcations correspond to a rearrangement of the dynamics in the characteristic space $\chi(X)$. They are defined by the crossing of two or more energy levels of the (orthogonal) structures as the parameter varies. We will see in the examples of Sections 4 and 5 how the global entropy defined in Section 2.2.1 is a good indicator of this type of bifurcation. As is wellknown, this type of bifurcation corresponds to an exchange of stabililty in the inertial axis of the dynamics in dynamical systems theory, or to an exchange of energy between different eddies or "coherent structures" in hydrodynamics. Recall that at least in finite dimension,(37) in the case where U is a continuously differentiable function of the parameter in some interval I, so are the eigenvalues and eigenfunctions of U^*U (of Section 1). It then makes sense to speak about the exchange of energy between dominant structures, since it is possible, in principle, to follow each structure (chrono and topo) through the bifurcation point. For infinite dimension, the situation is slightly more complex and the identification is possible only under certain conditions. We will come back to the description of internal bifurcations in the examples of the following sections.

We now illustrate the case of external bifurcations with some examples.

3.4.1. Period Doubling

A time periodic orbit of period K is defined by the K vectors of $L^2(X)$:

$$\xi_1, \xi_2, \ldots, \xi_K \tag{3.19}$$

When these vectors are linearly independent (which generically happens), $\chi(X)$ is likely to have dimension K. In the other case (with the presence of symmetries, for example), the dimension can be decreased. This is indeed true for the example treated in Section 4. Note that this point is independent of the possible complexity of each topo and chrono and it concerns only their number, that is, the dimension of $\chi(X)$ and the linear independence of vectors ξ_i, $i = 1, 2, \ldots, K$. It immediately follows that in general (i.e., in generic cases), period doubling leads to an increase of the characteristic dimension.

3.4.2. Supercritical Hopf Bifurcation

For a centered signal, this bifurcation in which a stable limit cycle emerges from a fixed point, the characteristic dimension jumps from 1 (or 0 in the particular case where the point is centered) to 3 (or 2 in the particular case where the cycle is in a plane), since the generic embedding dimension of a cycle is 3. Remark that the Liapunov dimension remains zero through the bifurcation, showing that in laminar cases, relation (3.17) may not be true.

3.4.3. Ruelle–Takens Scenario

Here, chaos arises after a sequence of Hopf bifurcations from a fixed point to a periodic orbit, which is followed by quasiperiodic motion on a two-dimensional torus. The characteristic dimension thus generically jumps from 1 (or 0 as explained in the previous paragraph) to 3 (or 2 as also explained in the previous paragraph), then from 3 (or 2) to 3 (or 4 as a torus is the Cartesian product of two cycles), leading to a strange attractor studied in Section 3.3. Note that the passage from a limit cycle to a T^2 torus may not correspond to a change of the characteristic dimension.

3.5. Infinite Dimensions

The von Neumann theory of comparison of infinite-dimensional projections(22) can be applied in order to generalize the previous analysis to the case of infinite dimensions. Note that the characteristic dimension can be defined in this context as

$$\dim(u) = \operatorname{tr}(G^*G) \tag{3.20}$$

where G is the partial isometry of Section 1.11, so that G^*G is a projection and tr a normalized trace. However, infinite dimensions are not very useful in our case, since practical signals ought to have finite characteristic dimensions even if they are initially defined in some infinite-dimensional space.

3.6. Spatial Analysis

It is clear from the space/time symmetry already described that the same analysis can be performed on the spatial structure of the solution. It leads, for example, to the description of space periodicity and the corresponding space bifurcations, as can be seen for example in coupled map lattices (see next section). It can also lead to the possibility of more "strange" symmetries in space which can be related, for instance, to convective waves which correspond to cycles in $\chi(T)$. Although this is not observed in both examples we analyze in the next sections, this is a common situation in hydrodynamics. The reduction of $\chi(T)$ to a (quasi) one-dimensional space is an indication of the rising of a (quasi) homogeneous configuration, as should be the case(8) for large spatial interaction in the coupled map lattice presented in the next section and some fluid flows. Here, we use the prefix "quasi" to account for the possibility of small fluctuations around the given property.

4. APPLICATION TO A COUPLED MAP LATTICE

Here and in the following section, we apply some of the concepts developed above to two examples: a coupled map lattice and an open fluid flow.

4.1. A Coupled Map Lattice

Coupled map lattices (CML) have been proposed as simple models for space-time complexity in one- or higher-dimensional spatially extended systems. By spatially coupling together dynamical systems on a lattice, they are a natural way to generate spatially large systems with many degrees of freedom which can produce various regimes going from regular motion (laminar states) to both spatial and temporal chaotic motion.

We restrict our study to the one-dimensional lattice, so that in our case a coupled map lattice is a time-dependent chain of maps, that is, a dynamical system with descrete time and space. Although different systems have been investigated (for example, refs. 17, 34, 38, and 69), we consider here the case where the coupling is of the diffusive type and concerns only nearest neighbors. The system is a lattice of N spatial discrete points i, evolving in time according to the following formula:

$$x_i^{n+1} = (1-\varepsilon) f(x_i^n) + \frac{\varepsilon}{2} [f(x_{i-1}^n) + f(x_{i+1}^n)] \tag{4.1}$$

where n is the discrete time index, ε the coupling parameter (which plays the role of a bifurcation parameter), and f a nonlinear map. Different maps are possible; we choose here the logistic quadratic map, which is known to have strong chaotic properties:

$$f(x) = ax(1 - x) \tag{4.2}$$

We take periodic boundary conditions, since they are the best adapted to simulate an extended (open) system. Also, we fix $a = 3.84$, since for this value of the parameter, the logistic quadratic map is known to have a chaotic dynamics that exchanges two intervals I_1 and I_2 of $[0, 1]$. A description of this extended system in this range of parameter is given in Bunimovich *et al.*(14) Here, we use the same initial condition in a systematic way. Our choice is a configuration with spatial period 8 defined by

$$x_i^0 = 0.75 + 0.22 \sin\left(\frac{2\pi}{8} i\right) \tag{4.3}$$

since the system then undergoes various bifurcations as ε varies.

In previous CML studies (see, for example, the complete study of Kaneko(34)), the distinction between various regimes is based on: (i) a qualitative description (for the phase diagram), (ii) space (or time) Fourier analysis and space-time Fourier analysis, (iii) characterization in "bit" space: definition of an "intermittency" function (in the turbulence community language). The function is zero or one depending on whether the signal amplitude is less or greater than a certain threshold value.

Instead, we use the biorthogonal decomposition (1.5) to analyze the space-time signals obtained at different values of the coupling parameter. Bifurcations were detected using the entropy defined in Section 2, and then carefully analyzed by direct computation of the dynamics as well as computing the different quantities defined in Sections 1 and 2. Here we present some of the regimes we have found, mainly focusing on the bifurcation points where a transition from one regime to another can be shown. Looking at Fig. 6, we can easily detect such points. Since the complete analysis of the bifurcation diagram is not the purpose of the present work, we present here only some typical cases. A complete description of the phase diagram of the CML from the point of view of the biorthogonal decomposition will be published elsewhere.

4.2. Application of the Biorthogonal Decomposition

The eigenvalues, topos, and chronos of Section 1 are computed for a large number of bifurcation parameter values (ε) in the following way:

(i) At each value of ε, the spatial correlation matrix given in (1.4) is computed over a number of time steps sufficiently large so that the matrix converges.

(ii) Eigenvalues and topos are then computed using the discretized form of Eq. (1.7).

(iii) Chronos are deduced by taking the scalar product of the signal and the topos. In some cases, instead, we use the temporal two-point correlation function and solve Eq. (1.10). Of course, both methods lead to identical results (Proposition 1.7 and Remark 1.9).

These computations include 200 (spatial) sites and 200 time points (taken after a transient time of 20,000 in most cases).

4.3. Chaotic Regime

This is the situation for small coupling, $\varepsilon \leqslant 0.07$, for which we know$^{(15)}$ that there is only one invariant measure, with exponential decay of correlations in both space and time. It is then natural to have a large characteristic dimension of the signal; for a centered signal the equirepartition of the energy among the chronos and topos is clearly present and therefore the global entropy is very large (close to 1); see Fig. 6.

The dynamics ξ_t fills a quasispherical (or isotropic) bounded region of the characteristic space $\chi(x)$. Conversely, the dispersion of the local signals η_X in $\chi(T)$ is uniform in a bounded isotropic region, as expected from the properties of the invariant measure.

The total energy, however, decreases very fast, in a continuous way, mainly due to the increase of diffusion as ε becomes larger (see Fig. 5).

The irregular shape of the chronos and topos can be observed in Fig. 1a.

4.4. Laminar Regime

At $\varepsilon = 0.08$ a bifurcation takes place to a periodic motion with period 4 in a three-dimensional phase space (up to very small deviations which become of the order of roundoff errors after a long transient). The entropy suddenly falls to a much lower plateau, below 0.09, where it roughly remains until $\varepsilon = 0.17$; see Fig. 6. In view of the discussion of Section 2.2.4, this is characteristic of an ordered regime where the energy is quasiconcentrated in the first structure. This is consistent with the appearance of order and coherence (standing waves) as described in Bunimovich *et al.*$^{(14)}$ and explained there by a symmetry $\varepsilon \leftrightarrow (1 - \varepsilon)$.

In this regime, the first eigenvalue α_1^2 is much greater than the others, showing that the dynamics is concentrated in a very narrow region along

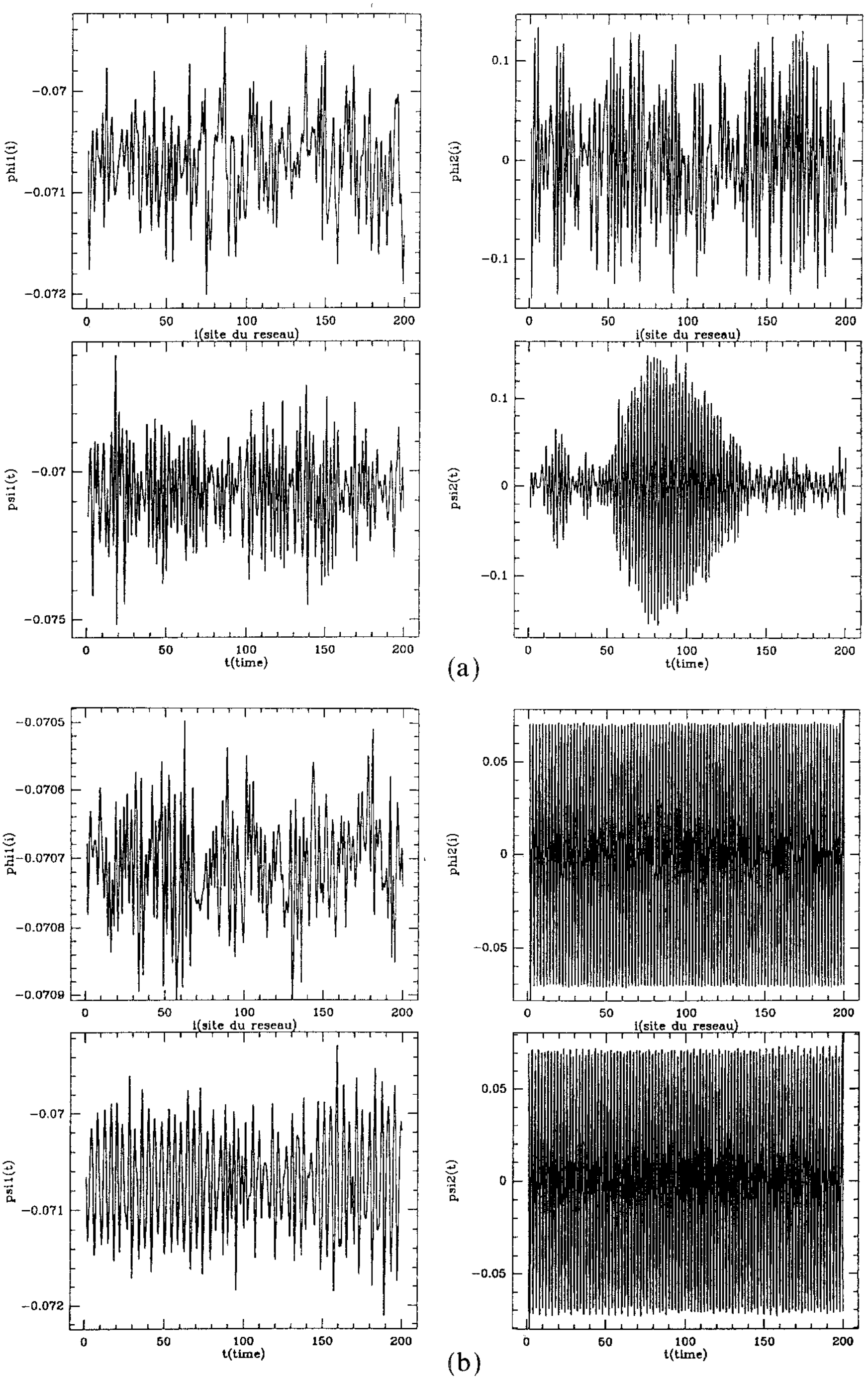

Fig. 1. Topos φ_k and chronos ψ_k for different coupling parameter values in CML (bifurcation from chaotic to laminar regime); (a) $\varepsilon = 0.06$ $[H(u) = 0.60,\ p_1 = 0.90,\ p_2 = 0.008]$; (b) $\varepsilon = 0.08$ $[H(u) = 0.079,\ p_1 = 0.89,\ p_2 = 0.099]$.

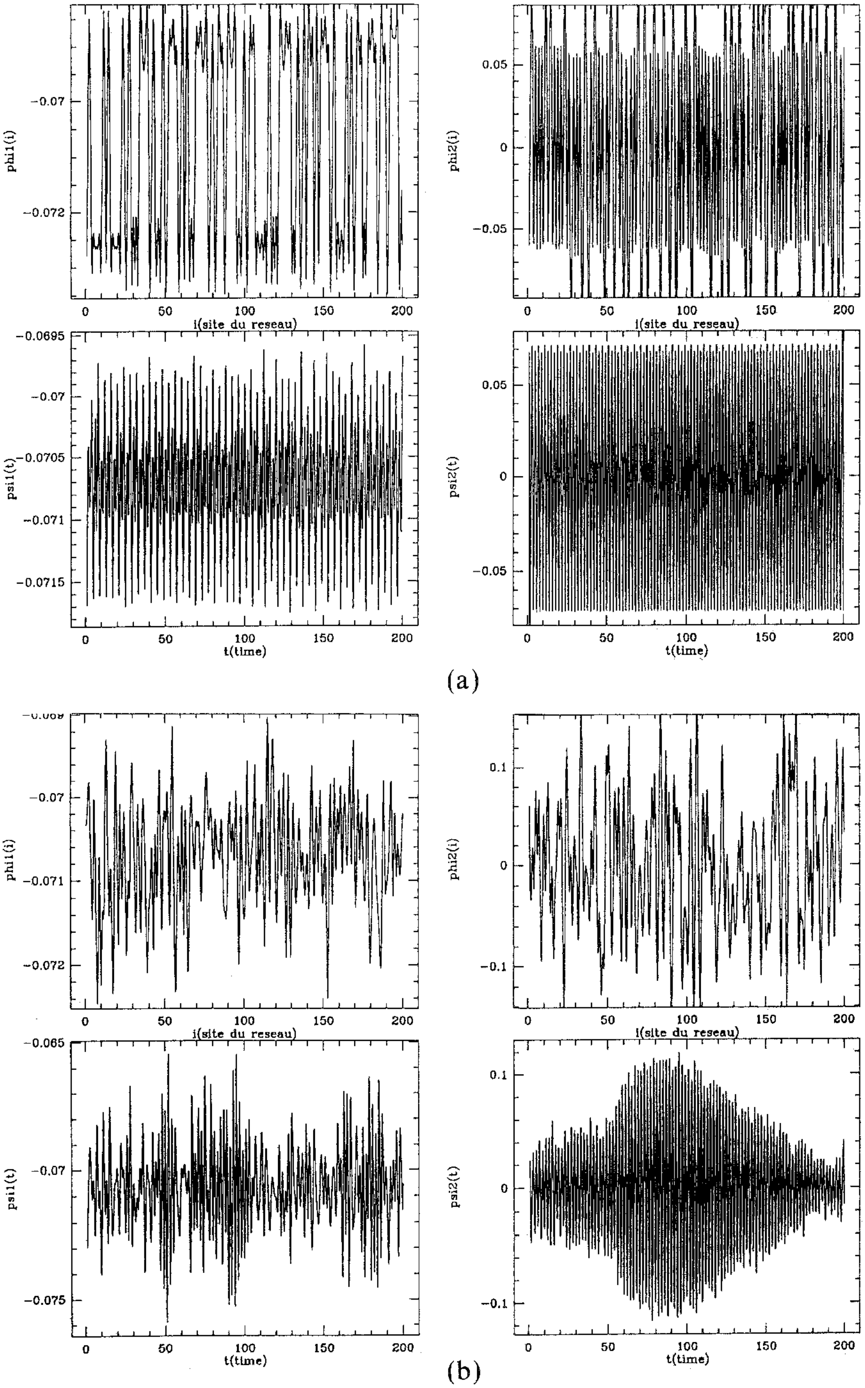

Fig. 2. Topos φ_k and chronos ψ_k for different coupling parameter values in CML (bifurcation from laminar to intermittent regime); (a) $\varepsilon = 0.17$ $[H(u) = 0.04,\ p_1 = 0.92,\ p_2 = 0.075]$; (b) $\varepsilon = 0.18$ $[H(u) = 0.54,\ p_1 = 0.90,\ p_2 = 0.017]$.

the direction φ_1 in $\chi(X)$. At $\varepsilon = 0.13$, every pair of points on the previous periodic orbit merge, given rise to a periodic orbit of period two in a two-dimensional phase space. This periodic orbit is present only in a very small range of the bifurcation parameter ε, another bifurcation taking place to a periodic orbit of period 4. Notice that this bifurcation can be detected from Fig. 4, but it is more difficult to see on the energy and entropy curves inside the range of precision of our measure.

4.5. Intermittency

For $0.18 \leqslant \varepsilon \leqslant 0.52$, the system displays a typical spatiotemporal intermittent dynamics. This regime is characterized, from our point of view, by successive crossings of the second and third eigenvalues (see Fig. 4), a phenomenon which also appears in the corresponding analysis of the experimental signal of Section 5.

Since the energy gets distributed among different modes, the entropy increases, and probably due to pattern competition in this intermittent regime, strong fluctuations are observed. For some values of ε, it is possible to relate local maxima and minima of the entropy with the crossing of eigenvalues (relative equirepartition) and the values of maximum eccentricity of the dynamic ellipsoid. We will come back to that phenomenon in more detail in Section 5, as it appears there more clearly.

The dynamics evolves in an ellipsoid with main axis φ_1 whose internal structure evolves itself in time. The main feature of this time-dependent motion is the rotation of the plane of the ellipse around φ_1, which can be detected by noticing that the second and third chronos on one hand (see Fig. 2b) and the third and fourth on the other hand (see Fig. 3a) alternate in time.

It is interesting to mention that for $\varepsilon = 0.18$ a more careful inspection of the dynamics in the 3-dimensional part $\varphi_1, \varphi_2, \varphi_3$ of the characteristic space shows the existence of a Silnikov$^{(61)}$ homoclinic loop which seems to drive the dynamics for this value of the parameter. We will come back to this special feature in subsequent work.

4.6. Laminar with Inverse Cascade

For $\varepsilon = 0.53$ the system suddenly becomes laminar. In this case, chronos and topos are periodic as shown in Fig. 3b. The entropy falls again to a low level (see Fig. 6), α_1 is much greater than α_2, and α_3 is almost 0 (Fig. 4). For $0.53 \leqslant \varepsilon \leqslant 0.66$ the dynamics has time period 4 in a characteristic space $\chi(X)$ which is two-dimensional, and for $0.66 \leqslant \varepsilon \leqslant 1$ the (time) period becomes 2 in a one-dimensional characteristic space. The bifurcation

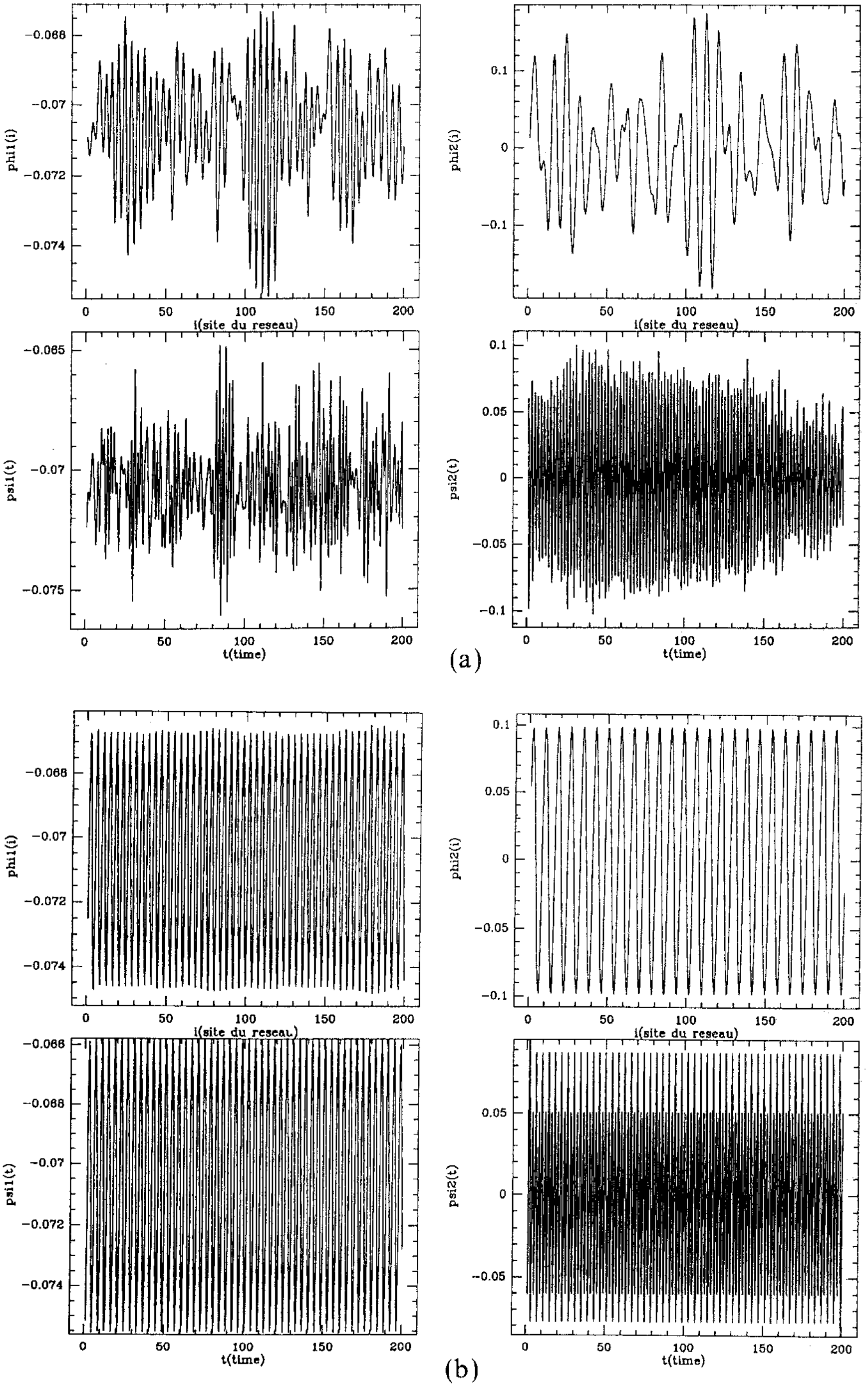

Fig. 3. Topos φ_k and chronos ψ_k for different coupling parameter values in CML (bifurcation from intermittent to laminar with inverse cascade regime); (a) $\varepsilon = 0.52$ $[H(u) = 0.52,$ $p_1 = 0.91,$ $p_2 = 0.023]$; (b) $\varepsilon = 0.53$ $[H(u) = 0.035,$ $p_1 = 0.93,$ $p_2 = 0.074]$.

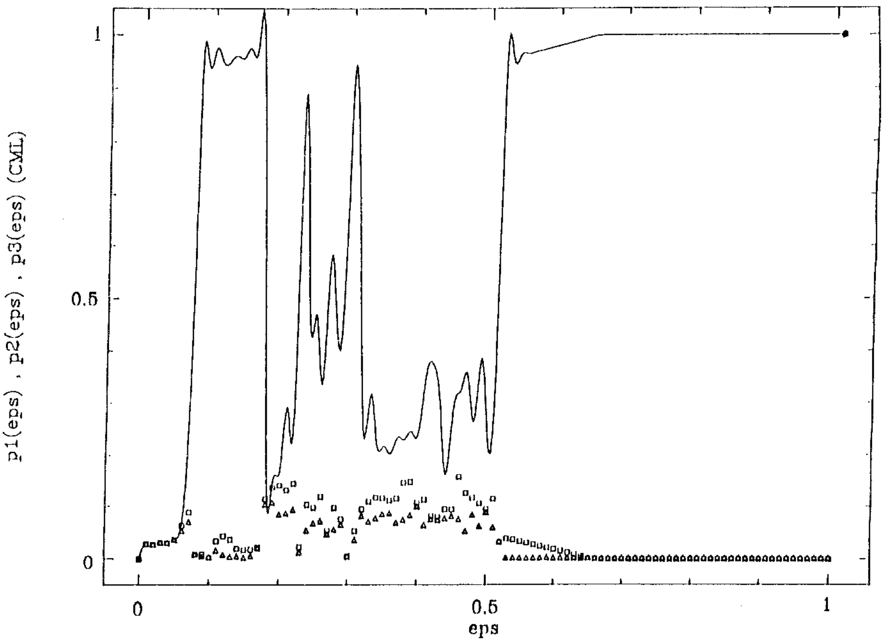

Fig. 4. Normalized eigenvalue α_k^2 for the temporally centered signal as a function of the parameter ε in CML for the first three structures: α_1^2 (---), α_2^2 ( ), α_3^2 (△ △ △).

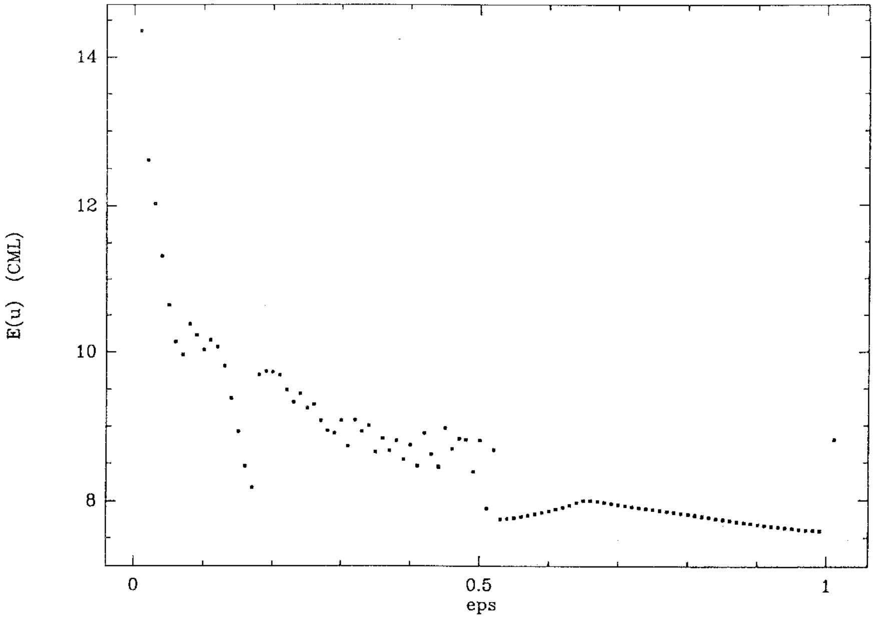

Fig. 5. Global energy as a function of the coupling parameter ε in CML.

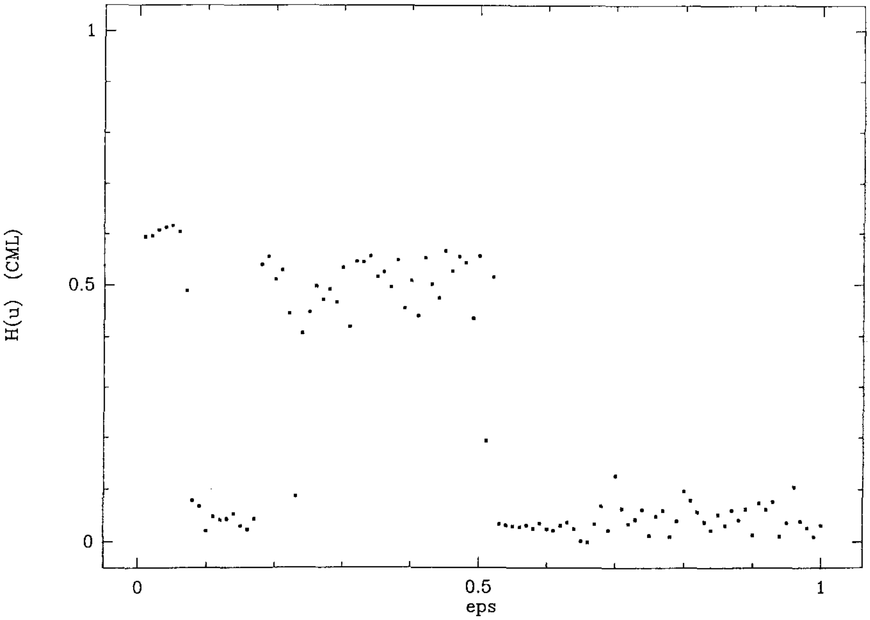

Fig. 6. Global entropy as a function of the coupling parameter ε in CML.

at $\varepsilon = 0.66$ is of the external type described in Section 3.4, since for $\varepsilon > 0.66$, α_2 is zero (Fig. 4), while it is nonzero for $\varepsilon < 0.66$ (Fig. 5). The fact that we do not recover the characteristic dimensions that generically correspond to these periods (2 and 4), as described in Section 3.4, is due to the symmetries of the model.(16) Finally, although only one inverse period-doubling bifurcation is shown here, we know, by either theoretical results(56) or our numerical results using different initial conditions, that a more complete picture of a period-doubling cascade arises in this range of parameter.

Finally, we can also mention that the energy suddenly drops at $\varepsilon = 0.53$ and has a relative maximum at $\varepsilon = 0.66$ (Fig. 5).

4.7. Concluding Remarks

It is clear that the above description is restricted to one initial condition and one valuer of the parameter in the logistic map. The entire phase space is known to be much richer (see, for example, Kaneko(34)). For instance, it is clear that a slight variation of the initial conditions would give a complete cascade of period doubling.(56) We have restricted ourselves somewhat like an experimentalist for whom it is not always possible to explore a full set of (initial) conditions for each value of the parameter.

Nevertheless, we have shown how the quantities defined in Sections 1 and 2, specifically the global energy and entropy of the biorthogonal decomposition, can be very useful for the distinction of various regimes in the coupled map lattice studied here. They both show discontinuities at bifurcation points as well as typical behaviors and thus can be used in the description of the dynamics of this model as well as a tool for bifurcation detection from complex numerical or experimental data.

5. APPLICATION TO A ROTATING DISK FLOW INSTABILITY

5.1. The Instability Problem

The stability of a rotating disk flow has been investigated in numerous numerical and experimental studies. The importance of this basic flow is due to the presence of a radial component of the mean (temporal) velocity that, combined with the azimuthal component, gives rise to a cross-flow inflection point and leads to the formation of spiral vortices in the transition regime. This phenomenon has been observed in several flow geometries, such as swept wings and rotating cones, in addition to a rotating disk. Smith(65) first observed sinusoidal waves in the transition regime, while Gregory *et al.*(30) later discovered spiral vortices. By visualizing the flow with a china-clay technique, they could measure the number of vortices appearing on the disk as well as the direction ε of the vortex axis inclined to the tangential direction. The linear stability analysis of the rotating boundary layer has been carried out by Gregory *et al.*(30) for the inviscid flow, by Brown(12) and Yamashita and Takematsu,(72) who included viscous effects, and by Kobayashi *et al.*(40) and Malik *et al.*,(49) who took into account the effect of streamline curvature and Coriolis force. These works predict the critical Reynolds number, the number of vortices, and their orientation ε.

While the above studies concern only the first instability from laminar flow (essentially the formation of spiral vortices), we are seeking a description and an understanding of physical phenomena in the full transition process, between the critical Reynolds number (at which the first instability occurs) and the transition Reynolds number (at the onset of turbulence).

5.2. The Experiment

Experimental facility, measurement techniques, and data acquisition are described in detail by Aubry *et al.*(3) We only give here a brief review. The experiment was carried out on a rotating disk 450 mm in diameter and 30 mm in thickness which was made of aluminum and mounted on a vertical axis. The disk stands in a plexiglass cylinder of diameter 800 mm, which itself lies in a large tank. The tank is filled with distilled water kept at constant temperature. We can define a local Reynolds number as $Re = r^2\omega/\nu$, where r is the distance from the center of the disk, ω the angular velocity of the disk, and ν the kinematic viscosity of the water. There are thus two ways to study the instability mechanism as Reynolds number increases: first, one can increase the rotation speed; second one can simply observe (or measure) the flow along a radius from the center to the periphery of the disk. When the disk rotates at a constant low angular velocity, the flow remains laminar everywhere on the disk. For a higher rotation speed, the flow stays laminar in the central region of the disk, but becomes unstable at a certain distance from the center. As the angular velocity is increased, the flow becomes turbulent at the periphery of the disk. Measurements with hot-film anemometry have been taken first with a fixed probe at various rotation speeds (experiment I), second with a moving probe at a constant angular velocity (experiment II). In the following, we analyze the experimental data of Aubry *et al.*[3]

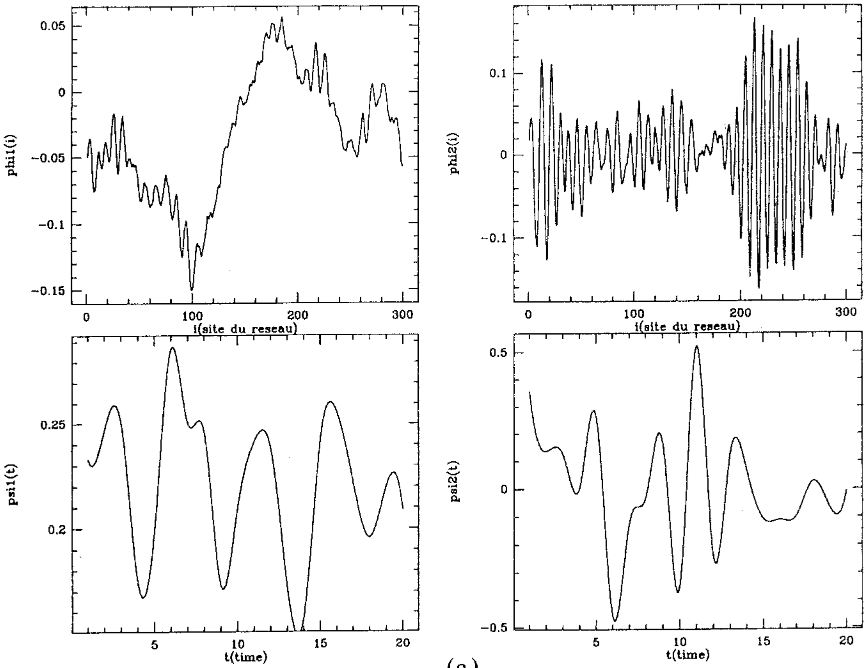

Fig. 7. Topos φ_k and chronos ψ_k of the biorthogonal decomposition applied to the rotating disk experiment I (see Section 5) computed with 20 disk rotations and 300 points on each rotation, for different Reynolds number Re: (a) $Re = 1.55 \times 10^5$ [$H(u) = 0.7$, $p_1 = 0.42$, $p_2 = 0.12$); (b) $Re = 1.77 \times 10^5$ [$H(u) = 0.8$, $p_1 = 0.26$, $p_2 = 0.16$]; (c) $Re = 2.40 \times 10^5$ [$H(u) = 0.9$, $p_1 = 0.11$, $p_2 = 0.10$].

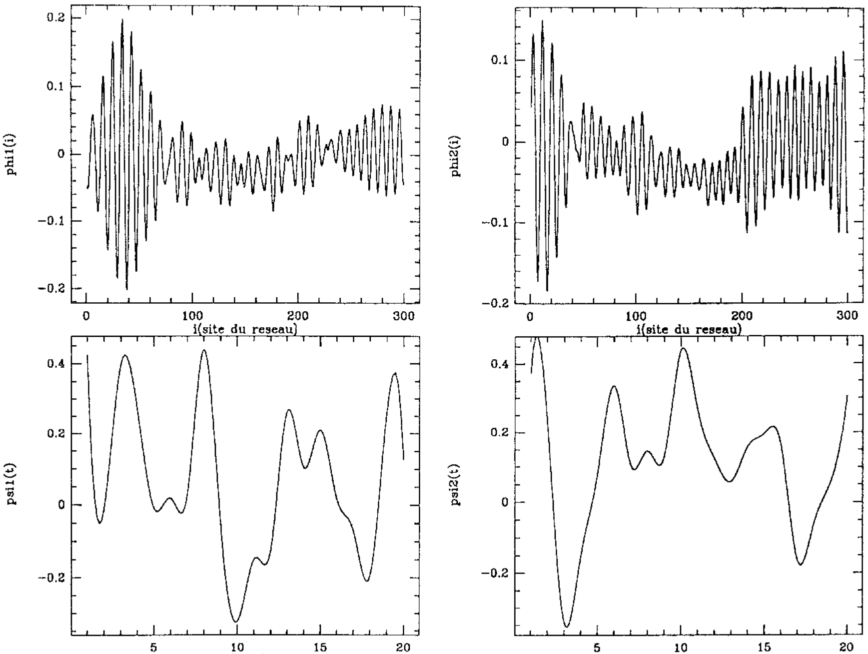

(b)

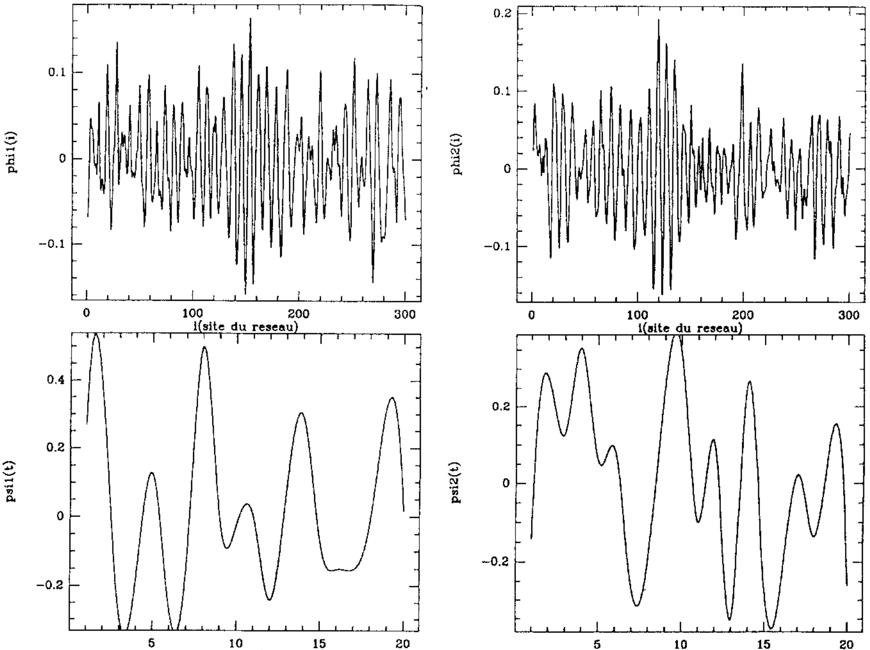

(c)

Fig. 7. (*Continued*)

5.3. Application of the Biorthogonal Decomposition

Since measurements have been obtained with a single probe, a real space-time signal $u(x, t)$ is not fully available. Such a signal was, however, artificially built by mapping the time variable over one rotation of the disk to a space variable. This is equivalent to dividing the signal $u(t)$ into windows, each window describing one disk rotation. The signal which we now analyze with the tools introduced in Sections 1 and 2 can be read as $u(i, j)$, where i is the index of the point on a disk rotation (inside the window) and j the index of the disk rotation. In the following, the index i is associated with the "space" variable x and the index j with the time variable t. The signal, in experiment I, contains 20 disk rotations (or time points) and 300 points on each rotation (or space points), while the signal in experiment II is formed with 15 time points and 512 space points. This number of data is varied in both cases (14 time points in both cases and

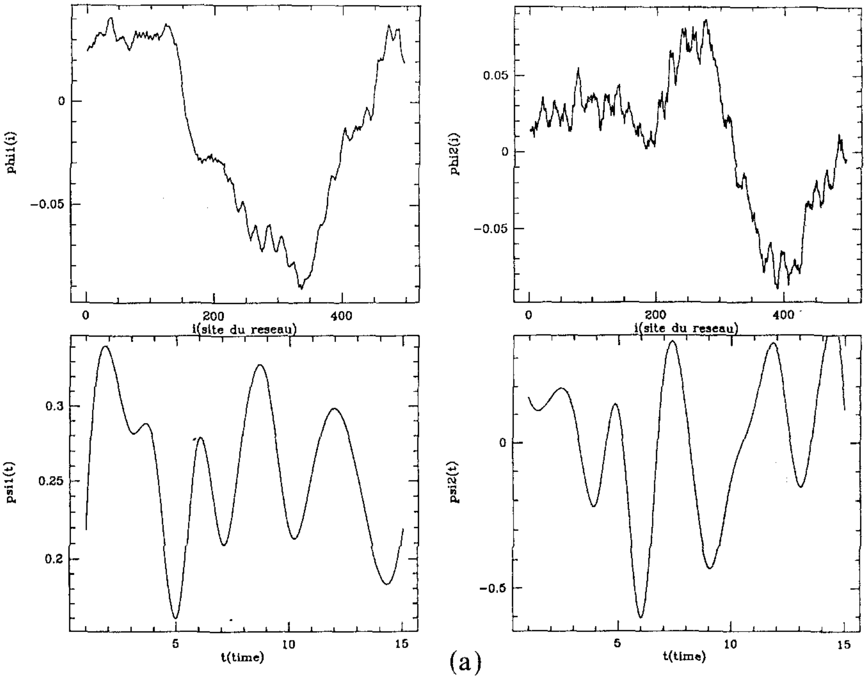

Fig. 8. Topos φ_k and chronos ψ_k of the biorthogonal decomposition applied to the rotating disk experiment II (see Section 5) computed with 15 disk rotations and 512 points on each rotation, for different Reynolds numbers Re: (a) $Re = 1.06 \times 10^5$ [$H(u) = 0.4$, $p_1 = 0.74$, $p_2 = 0.087$]; (b) $Re = 1.51 \times 10^5$ [$H(u) = 0.75$, $p_1 = 0.39$, $p_2 = 0.16$]; (c) $Re = 2.58 \times 10^5$ [$H(u) = 0.9$, $p_1 = 0.12$, $p_2 = 0.12$].

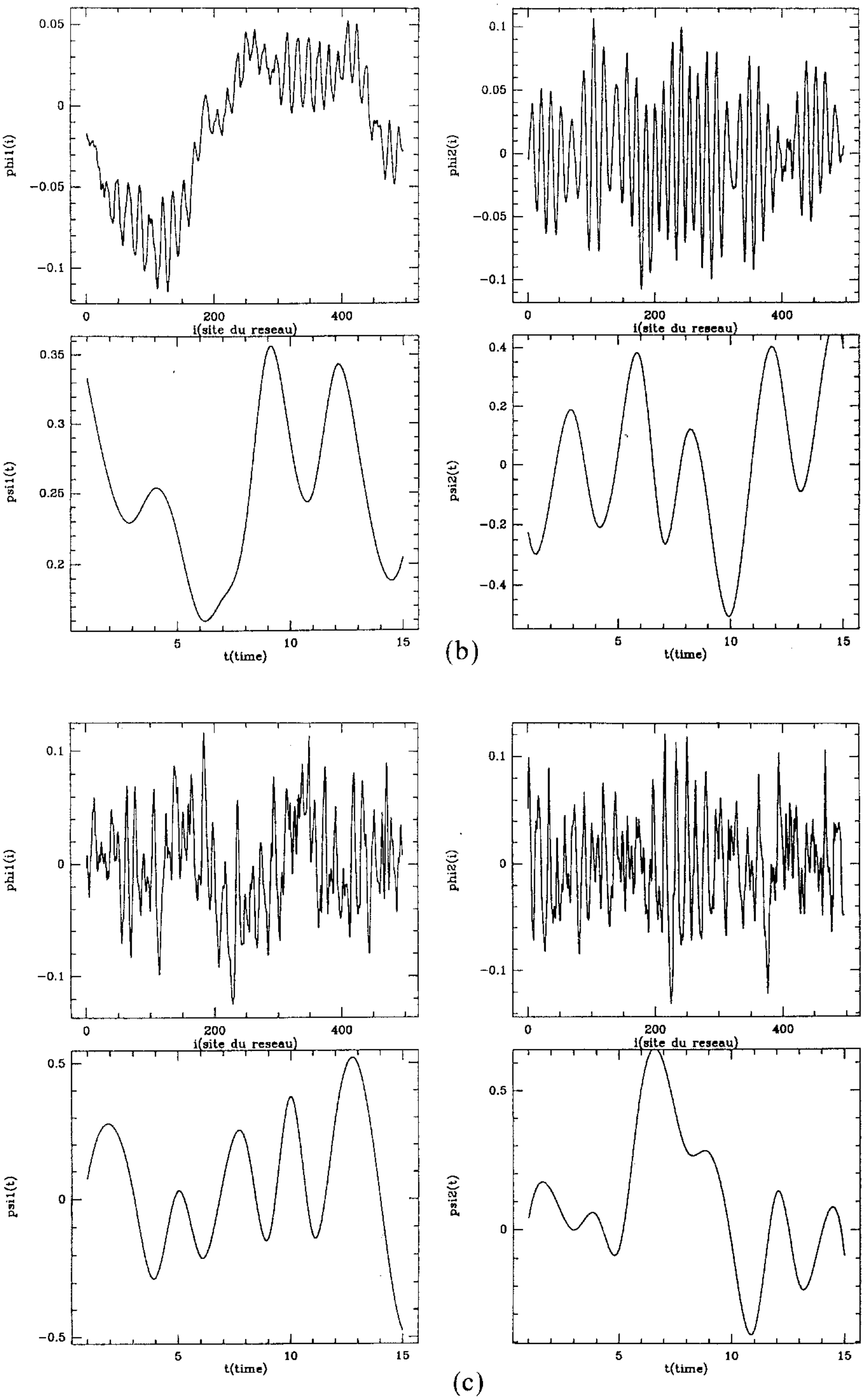

Fig. 8. (*Continued*)

256 space points in experiment II were retained), but the results are found to be extremely robust (see Aubry *et al.*[3] for more details).

We now compute the eigenvalues, topos, and chronos of the experimental signals as we did for the coupled map lattice in Section 4.2. The biorthogonal decomposition 1.5 is obtained for various Reynolds numbers in the transition range for the two sets of measurements I and II, and topos and chronos are shown in Figs. 7 and 8. As expected, the convergence of the series of eigenvalues decreases as Reynolds number increases, that is, although one or two terms are needed in the first stages of the transition regime, more and more terms become necessary as Reynolds number increases. Figures 9 and 10 present the relative energies p_1 and p_2 of the first two structures (represented by squares and triangles, respectively) and their evolution with Reynolds number, in experiments I and II. Since detailed structures depend on the specific experiment, we first concentrate on the first one (Fig. 9). On one hand, it is clear that the two curves $p_1(Re)$ abnd $p_2(Re)$ have discontinuity points at certain Reynolds numbers. On the other hand, it is possible to recover two continuous curves by judiciously joining squares and triangles: the first one consists of 2 squares, 4 triangles, 2 squares, 5 triangles, 2 squares, 2 triangles, and

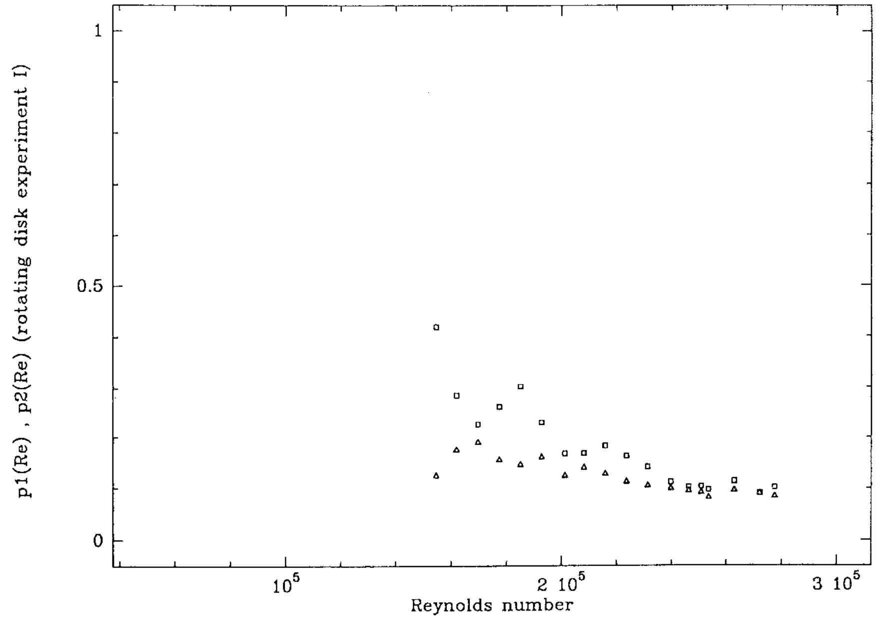

Fig. 9. Normalized energies of first and second structures, as a function of Reynolds number, in rotating disk experiment I. This illustrates the crossing of structures.

1 square, the second one is formed with 2 triangles, 4 suares, 2 triangles, 5 squares, 2 triangles, 2 squares, and 1 triangle. Each time these two continuous sets of points cross each other, the dominant structure becomes substructure and vice versa, showing how various instabilities take place in the transition process. The first crossing, for example, can be easily understood: at low Reynolds number, the first mode, namely a low-frequency noise due to the rotation of the disk, contains an important part of the energy. As the spiral vortices, presumably the second mode, develop through a (first) flow instability, they gaini energy and eventually overcome the low-frequency motion at $Re = 1.63 \times 10^5$. Similar findings can be made in experiment II from the analysis of Fig. 8. There, the first continuous curve is formed by 5 squares, 2 triangles, 3 squares, and 2 triangles and the second one by 5 triangles, 2 squares, 3 triangles, and 2 squares. We will come back to these important structure crossings by analyzing global entropy variations.

5.4. Global Characteristics of the Signals

We now report the global characteristics of the experimental signals and show the global energy and entropy in Figs. 11 and 12, respectively.

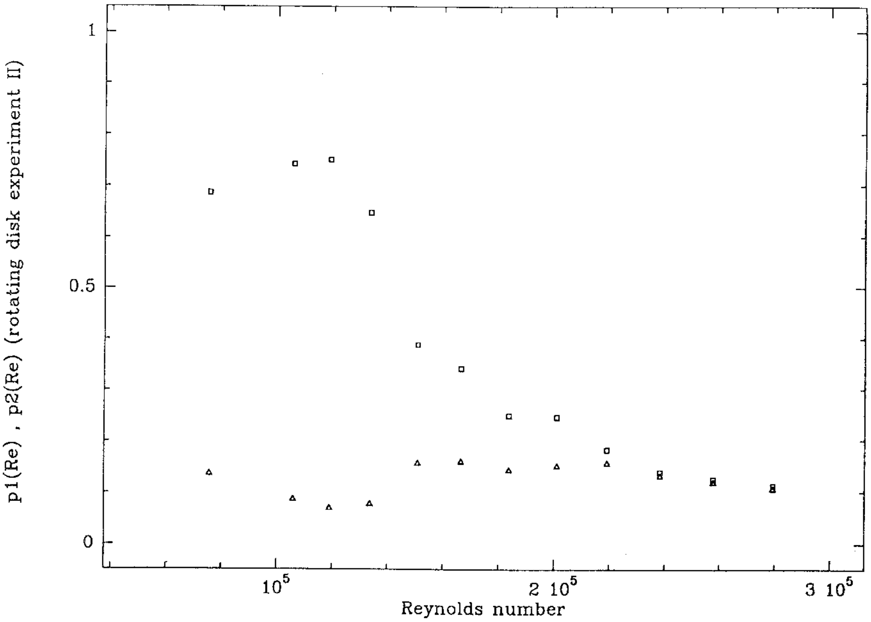

Fig. 10. Normalized energies of first and second structures, as a function of Reynolds number, in rotating disk experiment II. This again illustrates the crossing of structures.

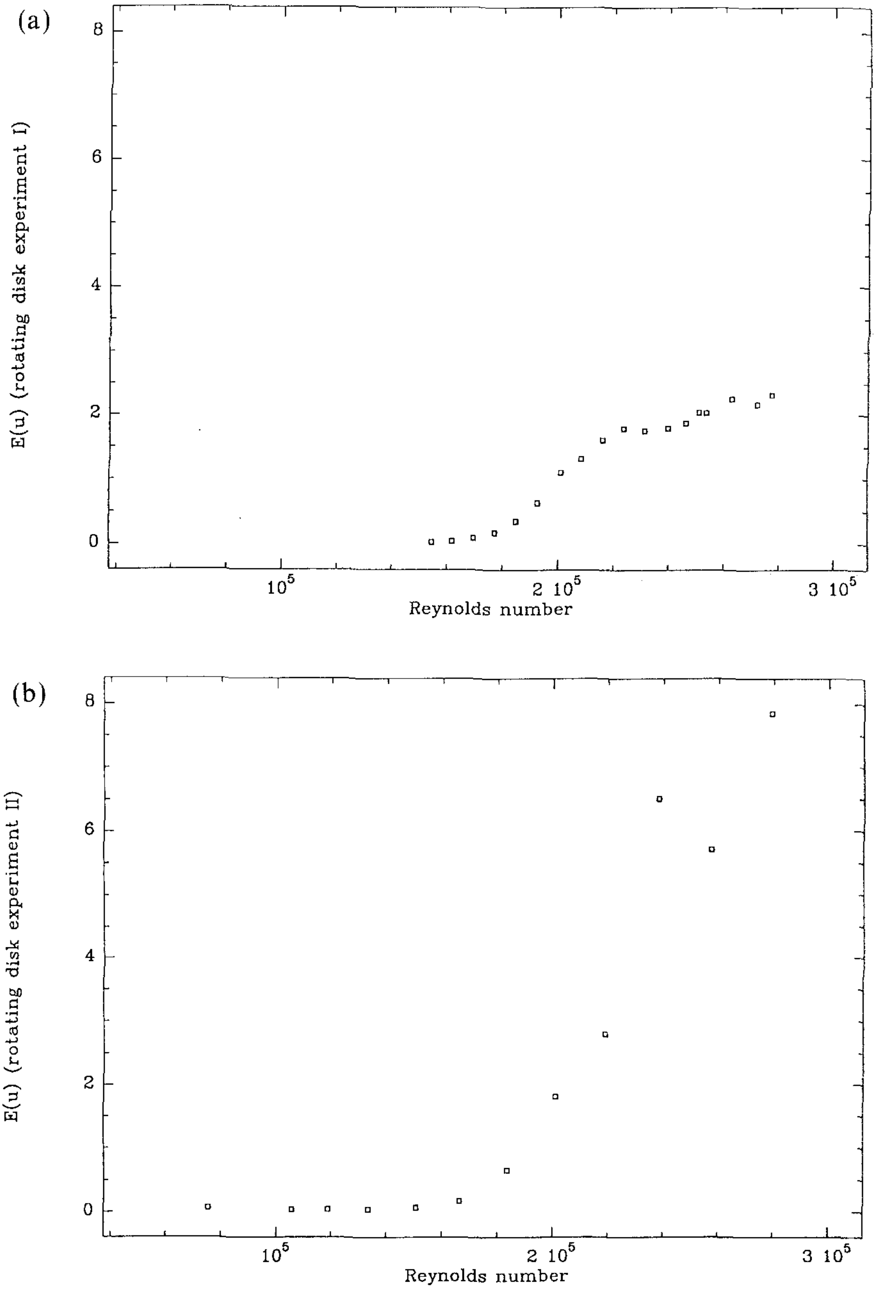

Fig. 11. Global energy as a function of Reynolds number in rotating disk experiment: (a) experiment I, (b) experiment II.

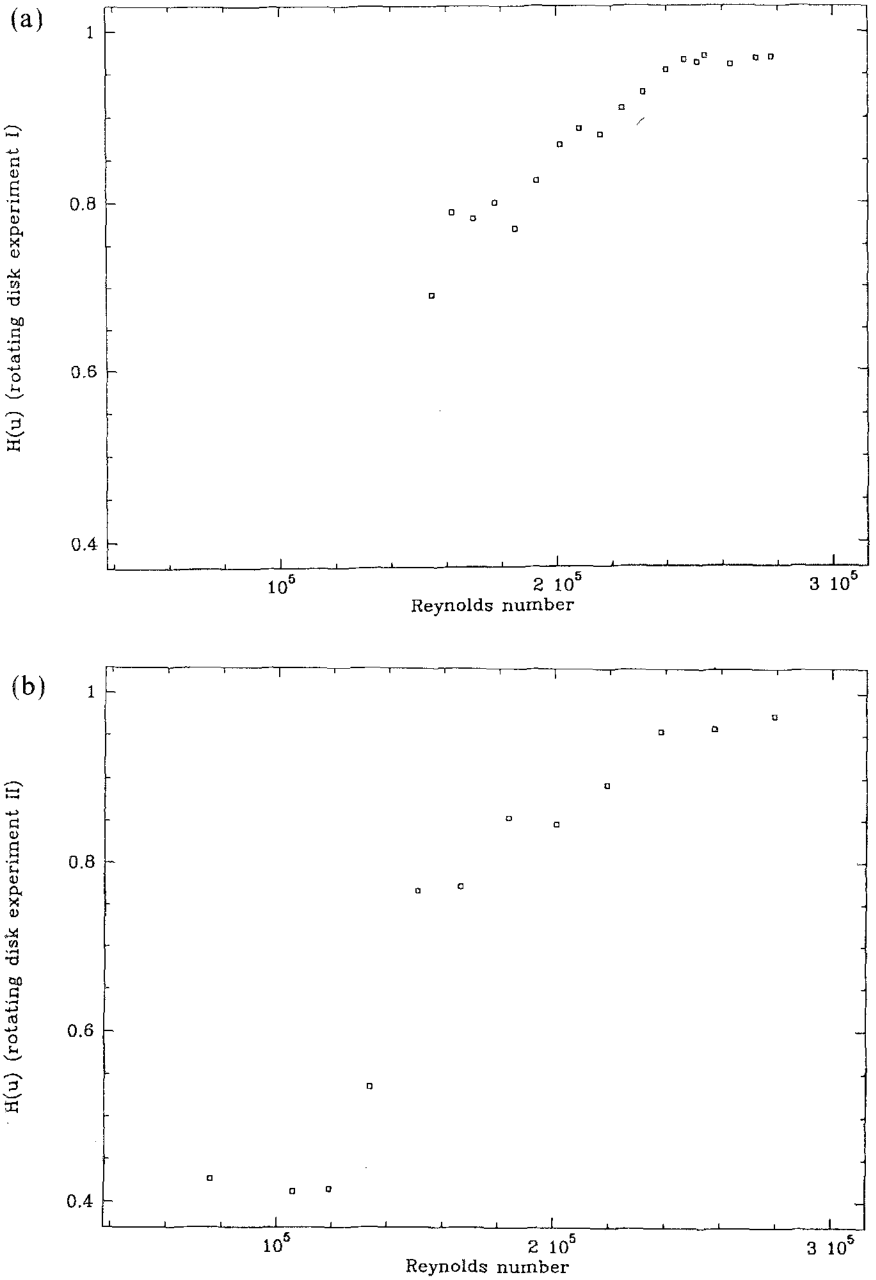

Fig. 12. Global entropy as a function of Reynolds number in rotating disk experiment: (a) experiment I, (b) experiment II.

In both experiments, the energy remains at a low level (close to zero) and starts increasing at the first mode crossing at $Re = 1.63 \times 10^5$. It then becomes larger and larger as Reynolds number increases, the increase being much faster in experiment II than in experiment I. In the following, we concentrate on the global entropy, which presents some interesting features. As expected, it tends to increase as Reynolds number gets higher, which is consistent with a route to turbulence corresponding to the generation of disorder or chaos. Nevertheless, more careful observation shows that short decreasing phases succeed more important increasing periods, a phenomenon that we now describe.

First, we notice that the entropy as a function of Reynolds number can be considered as a series of curves which are monotonically increasing, reach a local maximum, and slightly decrease until a local minimum which plays the role of starting point turbulent domain, the rate of entropy increase is significantly reduced (since it is already close to 1). Thus, the entropy rise from a level close to 0 to 1 (the most disordered case) takes place before the transition Reynolds number.

We now study entropy variations and start with experiment I (Fig. 12a). Let us number the points from 1 to 18 in Fig. 12a (from left to right). We note that the local maxima between points 2 and 3, 8 and 9, 13 and 14, 15 and 16, and 17 and 19 coincide with the mode crossings of Fig. 9 and the local minima occur when the modes are the furthest apart. (The lack of coincidence between points 4 and 5 is explained by a 3/4 mode crossing—instead of a 1/2 mode crossing—which has been observed, but we do not report it here.) This can be understood in the following way. When two structures are in competition, the energy is equally distributed among them: the entropy reaches a local maximum; after the overtaking of the substructure which has become the dominant one, the energy of the loser drops very fast and the entropy reaches a local minimum. From that point, the same phenomenon occurs again: another structure starts gaining energy, the entropy increases again until a new local maximum, etc. Note that the two competitive structures may be different or the same as Reynolds number increases. Local maxima of entropy are thus very useful for detecting mode crossings, i.e., various "instabilities" in the flow.

Let us suppose that on an interval $J_1 = [Re_1, Re_2]$ (so that H has local minima at Re_1 and Re_2), mode crossing concerns the first two structures only and that the energy of the other structures stays constant (in a first approximation). Letting C be

$$C = \sum_{k>2} p_k \tag{5.1}$$

we can write the relative energy of the second structure p_2 in terms of p_1 and C:

$$p_2 = 1 - p_1 - C \tag{5.2}$$

Since the sum of all the p_k is equal to 1, we can write the entropy as function of Reynolds number:

$$H(Re) = -p_1 \log p_1 - (1 - p_1 - C) \log(1 - p_1 - C) - D \tag{5.3}$$

where D represents the (approximately constant) sum of entropies of all the structures, except the first and second ones. The Reynolds number dependence of the right-hand side of Eq. (5.3) is (approximately) contained in p_1. The function $H(Re)$ on the successive Reynolds number intervals (defined with local entropy minima) satisfies (5.3). However, as Reynolds number increases, p_1 becomes smaller and C larger.

The same correspondence between entropy local maxima and structure crossings can be observed in the results of experiment II given in Fig. 12b. If we number the points from 1 to 12 from left to right, we can easily see that local entropy maxima occur between points 5 and 6, points 7 and 8, and points 10 and 11. These correspond exactly to 1/2 mode crossings observed ini Fig. 10 and previously commented upon.

5.4.3. Physical Interpretation

In experiment I, where the probe was moved and the angular velocity of the disk kept constant, the first instability was seen to occur at $Re_{c1} = 1.20 \times 10^5$ and transition to turbulence to take at $Re_{t1} = 2.77 \times 10^5$. In experiment II, where the probe was fixed and the disk rotation speed varied, we found a critical Reynolds number $Re_{c2} = 1.10 \times 10^5$ and a transition Reynolds number of $Re_{t2} = 2.79 \times 10^5$. Both experiments give thus approximately the same values for critical and transition Reynolds numbers and they are consistent with other values reported in the literature, which can be found, for example, in Malik *et al.*(49) (though here is considerable controversy). Moreover, we found that the Reynolds number at which the patterns born through the (first) instability become the most energetic (at the first local entropy maximum) is the same in both experiments: $Re = 1.63 \times 10^5$. The concept of this (third) Reynolds number may be interesting and should be investigated further.

It is well known that the first instability leads to the formation of spiral vortices. Although we have not proved it yet, it is likely that our first biorthogonal structure indeed represents these vortices after the first structure crossing has occurred. In fact, these vortices appear also in a

Fourier analysis, as shown by Aubry *et al.*,(3) who have plotted the Fourier power spectrum: the frequency characteristic of the developing instability corresponds to the number of spiral vortices (around 32) observed in experiments. It is interesting to not that the first structure crossing found in our analysis via the biorthogonal decomposition coincides with the Fourier mode crossing observed in the Fourier spectrum. If the Fourier analysis is useful in this first stage of the instability, it soon becomes useless as a thick packet of wave numbers gets activated.

6. SUMMARY AND CONCLUSION

To conclude, we have rigorously shown that any spatiotemporal (scalar or vectorial) signal can be decomposed into spatial and temporal orthogonal modes. This has been achieved in terms of the spectral analysis of an operator defined from the space of spatial signals to that of temporal ones. We were then able to describe some features of the information contained in the signal in terms of spectral properties. This allowed some effective computations of global quantities related to this specific analysis as well as some bounds of these quantities.

A remarkable property of the decomposed form of the signal is the association of each space component (which we call a topo) with a time component partner (which we call a chrono). The latter gives the time evolution of the former and the former is the spatial configuration of the latter.

In a simpler—but perhaps more abstract—way, we can think of the biorthogonal decomposition as a convenient change of variables in the phase space of the underlying dynamical system. From this viewpoint, we proposed to detect and analyze some of the possible changes (i.e., bifurcations) in the dynamical regime as some parameter varies. We argue that the detection of some bifurcations is often easier (and in some cases only possible) in such a system of coordinates.

The essential ingredients which carry this analysis in a simple way are: (1) the separation of time and space components, (2) the low dimension of the characteristic space inside the phase space where the signal effectively lies, and (3) the location inside that space of a bounded region where the dynamics stays most of the time.

A system of a coupled map lattice and an open fluid flow were then used as grounds for the application of the concepts and techniques previously developed. Despite the fact that we used some preliminary data in both examples which will require some further investigations, we hope to have illustrated our method and convinced the reader how useful this bridge between statistics and dynamics can be for the analysis of numerical or experimental data.

Finally, having in mind the examples treated above, we can trust that these ideas might be of some help in the study of systems displaying complex space-time dynamics.

ACKNOWLEDGMENTS

One of us (N.A.) expresses her sincere gratitude to her colleagues for their hospitality during her visit at Centre de Physique Théorique, where this research was initiated. She also gratefully acknowledges the support of NSF/PYI award MSS89-67462. One of us (R.L.) expresses his gratitude to ISI Foundation for their kind hospitality at Torino as well as to the participants of the workshop "Complexity and Evolution" for useful discussions, during the time when he worked on this paper.

REFERENCES

1. R. J. Adrian, *Phys. Fluids* **22**:2065 (1979).
2. R. J. Adrian, *Appl. Opt.* **23**:1690 (1984).
3. N. Aubry, M. P. Chauve, and R. Guyonnet, Analysis of a rotating disk flow experiment, Preprint, B. Levich Institute, CCNY of CUNY, New York, New York (1990).
4. N. Aubry, P. Holmes, J. L. Lumley, and E. Stone, *J. Fluid Mech.* **192**:115 (1988).
5. N. Aubry and S. Sanghi, in *Organized Structures and Turbulence in Fluid Mechanics*, M. Lesieur, ed. (Kluwer Academic, 1989).
6. V. I. Arnold, *Bifurcations and Singularities in Mathematics and Mechanics, Theoretical and Applied Mechanics*, P. Germain, M. Piau, and D. Caillerie, eds. (Elsevier, 1989).
7. A. V. Babin and M. I. Vishic, *Uspekhi Mat. Nauk* **38**:133 (1983) [*Russ. Math. Surv.* **38**:151 (1983)].
8. L. Batiston, L. Bunimovich, and R. Lima, Robustness of quasi-homogeneous configurations in coupled map lattice, Preprint, Institute for Scientific Interchange, Turin, Italy (1990).
9. P. Bergé, *Nucl. Phys. B* **2**:247 (1987).
10. P. Bergé, M. Dubois, P. Manneville, and Y. Pomeau, *J. Phys. Lett.* (Paris) **41**:L341 (1980).
11. R. F. Blackwelder and R. E. Kaplan, *J. Fluid Mech.* **76**:89 (1976).
12. W. B. Brown, in *Boundary Layer and Flow Control*, G. V. Lachmann, ed. (Pergamon Press, 1961), p. 913.
13. L. Bunimovich, *Sov. J. Theor. Exp. Phys.* **89**:4 (1985).
14. L. Bunimovich, A. Lambert, and R. Lima, *J. Stat. Phys.* **61** (1990).
15. L. Bunimovich and Ya. G. Sinai, *Nonlinearity* **1**:491–516 (1988).
16. B. Cantwell, *Annu. Rev. Fluid Mech.* **13**:453 (1981).
17. H. Chaté and P. Manneville, *C. R. Acad. Sci.* **304**:609 (1987); *Phys. Rev. A* **38**:4351 (1988); *Physica D* **32**:409 (1988).
18. S. Ciliberto, F. Francini, and F. Simonelli, *Opt. Commun.* **54**:251 (1985).
19. S. Ciliberto and P. Bigazzi, *Phys. Rev. Rev.* **60**:286 (1988).

20. S. Ciliberto and B. Nicolaenko, Estimating the number of degrees of freedom in spatially extended systems, Preprint, Instituto Nazionale di Ottica, Largo Enrico Fermi 6, 50125 Arcetri-Firenze, Italy (1990).
21. I. P. Cornfeld, S. V. Fomin, and Ya. G. Sinai, *Ergodic Theory* (Springer, 1980).
22. J. Dixmier, *Les Algèbres d'Opérateurs de l'Espace Hilbertien* (*Algèbre de von Neumann*) (Gauthiers-Villars, 1968).
23. M. J. Feigenbaum, *J. Stat. Phys.* **19**:25 (1978).
24. A. Fincham and R. Blackwelder, *Bull. Am. Phys. Soc.* (42nd Annu. Mtg. Div. Fluid Dynam.) **1989**:2266.
25. C. Foias, G. R. Sell, and R. Témam, *J. Differential Equations* **73**:309–353 (1988).
26. M. N. Glauser, S. J. Leib, and W. K. George, *Turbulent Shear Flows 5* (Springer-Verlag, 1987).
27. B. Gnedenko, *The Theory of Probability* (MIR, Moscow, 1976).
28. J. P. Gollub and H. L. Swinney, *Phys. Rev. Lett.* **35**:927 (1975).
29. P. Grassberger and I. Procaccia, *Physica* **9D**:189 (1983).
30. N. Gregory, J. T. Stuart, and W. S. Walker, *Phil. Trans.* **248**:155 (1955).
31. J. Guckenheimer and P. Holmes, *Nonlinear Oscillations, Dynamical Systems, and Bifurcations of Vector Fields* (Springer-Verlag, 1983).
32. J. C. R. Hunt, *Trans. Can. Soc. Mech. Eng.* **11**:21 (1987).
33. A. K. M. F. Hussain, *J. Fluid Mech.* **173**:303 (1986).
34. K. Kaneko, *Physica* **34D**:1 (1989).
35. J. L. Kaplan and J. A. Yorke, in *Functional Differential Equations and Approximations of Fixed Points*, H. O. Peitgen and H. O. Walther, eds. (Springer, Berlin, 1979), p. 204.
36. K. Karhunen, *Ann. Acad. Sci. Fenn. A1, Math. Phys.* **37**:1 (1946).
37. T. Kato, *Perturbation Theory for Linear Operators* (Springer-Verlag, 1966).
38. D. Keller and J. D. Farmer, *Physica* **23D**:842 (1986).
39. B. Khalighi, *Exp. Fluids* **7**(2):142 (1989).
40. R. Kobayashi, Y. Kohama, and Ch. Takamadate, *Acta Mech.* **35**:71 (1980).
41. A. N. Kolmogorov, *Dokl. Akad. Nauk SSSR* **30**:301 (1941).
42. A. Libchaber, C. Laroche, and S. Fauve, *J. Phys. Lett.* (Paris) **43**:L211 (1982).
43. H. W. Liepmann and R. Narisimha, eds., *Turbulence Management and Relaminarisation* (Springer-Verlag, 1987).
44. M. Loève, *Probability Theory* (Van Nostrand, 1955).
45. J. L. Lumley, in *Atmosdpheric Turbulence and Radio Wave Propagation*, A. M. Yaglom and V4. I. Tatarski, eds. (Nauka, Moscow, 1967), p. 166.
46. J. L. Lumley, *Stochastic Tools in Turbulence* (Academic, Press, 1972).
47. J. L. Lumley, in *Transition and Turbulence*, R. E. Meyer, ed. (Academic Press, 1981), p. 215.
48. J. L. Lumley, in *Whither Turbulance*?, J. L. Lumley, ed. (Springer-Verlag, 1990), p. 49.
49. M. R. Malik, S. P. Wilkinson, and S. A. Orszag, *AIAA J.* **19**:1131 (1981).
50. Mallet-Paret, *J. Differential Equations* **22** (1976).
51. R. Mañe, *Lecture Notes in Mathematics*, Vol. 898 (Springer, 1981).
52. J. Marsden, *Bull. AMS* **79**:537 (1973).
53. S. E. Newhouse, D. Ruelle, and F. Takens, *Commun. Math. Phys.* **64**:35 (1978).
54. Y. Pomeau and P. Manneville, *Commun. Math. Phys.* **101**:189 (1980).
55. Y. Pomeau, *Physica D* **23**:3 (1986).
56. A. I. Rakhmanov and N. K. Rakhmanova, On one dynamical system with spatial interactions, Preprint, Keldysk Institute for Applied Mathematics, Moscow (1990).
57. J. D. Rodriguez and L. Sirovich, *Physica D* **43**:77–86 (1990).
58. A. Roshko, *AIAA J.* **14**:1344 (1976).

59. D. Ruelle, *Chaotic Evolution and Strange Attractors* (Cambridge University Press, 1989).
60. D. Ruelle and F. Takens, *Commun. Math. Phys.* **20**:176 (1971).
61. L. P. Silnikov, *Sov. Math. Dokl.* **6**:163–166 (1965); *Math. USSR Sbornik* **6**:427–438 (1968), **10**:91 (1970).
62. L. Sirovich, *Q. Appl. Math.* **45**:561–590 (1987).
62. L. Sirovich, in *Proceedings 1989 Newport Conference on Turbulence* (Springer-Verlag).
63. L. Sirovich and A. E. Deane, A computational study of Rayleigh–Bénard convection. Part 2: Dimension considerations, Preprint, Brown University Center for Fluid Mechanics, Providence, Rhode Island.
64. C. R. Smith and R. D. Paxton, *Exp. Fluids* **1**:43 (1990).
65. N. H. Smith, NACA Tech. Note No. 1227 (1947).
66. F. Takens, *Lecture Notes in Mathematics* (Springer-Verlag, 1981), p. 898.
67. R. Témam, *Infinite Dimensional Dynamical Systems in Mechanics and Physics* (Springer-Verlag, New York, 1988).
68. H. Tennekes and J. L. Lumley, *A First Course in Turbulence* (MIT Press).
69. I. Waller and R. Kapral, *Phys. Rev.* **30A**:2047 (1984).
70. J. M. Wallace and F. Hussain, *Appl. Mech. Rev.* **43**:S203 (1990).
71. W. W. Willmarth, in *Advances in Applied Mechanics 15* (Academic Press, 1975), p. 159.
72. I. Yamashita and M. Takematsu, *Rep. Inst. Appl. Mech. Hyushu Univ.* (Japan) **22**(69) (1974).
73. S. Ciliberto and M. Caponeri, *Phys. Rev. Lett.* **1990**:2775–2778.
74. S. Ciliberto, in *Proceedings Les Houches, Complexity and Dynamics* (1990), to appear.
75. A. E. Deane, I. G. Kevrekidis, G. E. Karniadakis, and S. A. Orszag, Low dimensional models for complex flows geometry flows: Application to grooved channels and circular cylinders, Preprint (1990).
76. M. Kirby, D. Armbruster, and W. Güttinger, An approach for the analysis of spatially localized oscillations, in *Conference Proceedings: Bifurcations and Chaos*, Würzburg (to appear).